

Department of Physics
Ludwig-Maximilians-University Munich

Master Thesis in Physics
submitted by

Robin Eberhard
born in Aalen, Germany

handed in on

October 16, 2020

Spin Selective Imaging of Ground State Potassium Atoms

This Master Thesis has been carried out by Robin Eberhard at the
Physics Institute in Munich
under the supervision of
Prof. Dr. Christian Gross

should
this be Im-
manuel?

Spin Selective Imaging of Ground State Potassium Atoms

Robin Eberhard

Abstract

Abstract

Zusammenfassung

Abstract

Contents

1. Introduction	1
2. Loading atoms into optical tweezers	3
2.1. Theory on Polarization	4
2.2. Electro-optical modulators	5
2.2.1. Pockels effect	6
2.2.2. Driving a Pockels cell	8
2.2.3. Testing and evaluating pockels cells	11
3. Sorting of atoms	17
3.1. Acousto-optically deflected tweezers	17
3.1.1. Acousto-optical effect	18
3.1.2. Preparation of the tweezers beams	21
3.1.3. Moving tweezers	22
3.1.4. Tweezer homogeneity	23
3.2. Sorting algorithms	24
3.2.1. Pathfinding	25
3.2.2. Compression	25
3.2.3. Comparison of the two algorithms	26
3.3. Driving an RF-synthesizer for arbitrary pattern generation	27
3.3.1. Functionality of the Spectrum driver	28
3.3.2. Limits of using the card in the experiment	30
3.4. Conclusion	33
4. State selective light shifts for spin-sensitive imaging	43
4.1. Approaches	44
4.1.1. Zeemann induced potential separation	44
4.1.2. Utilization of state selective light shifts	46
4.2. Setup	49
4.2.1. Laser classification	49

4.2.2. Beam setup of spin-selective laser	50
4.2.3. Cavity classification	51
5. Conclusion and Outlook	55
A. Cavity for frequency stability of spin-sensitive tweezer	57
B. PDH lock of cavity	59

1. Introduction

Quantum mechanics provided a new way of thinking about physics and experimentalists and theorists have worked together in the last century, to validate this understanding. Nowadays, within the realm of quantum research, atoms are being controlled in an isolated environment, that have allowed to set e.g. new high-precision time standards [1] and resolve new types of matter [2, 3]. The scope of these studies has exponentially expanded over the last 30 years, as laser-cooling, trapping and detection techniques have gained momentum. Within this realm, the field of quantum simulation is of particular interest to this thesis, where microscopic effects found in solid state physics are modelled by arranging and interacting atoms on a macroscopic scale. Forming the structures necessary to measure effects in this regime, such as Ising [4] or Hubbard [5] models, is achieved by confining atoms to periodic potential wells in optical lattices.

Advancements in detection of atoms have lead to quantum gas microscopes [6, 7], where single-site resolutions in these lattices is possible and are thus a perfect fit for use in quantum simulators. This has allowed to measure e.g. superfluid to Mott insulator transitions [7] or antiferromagnetic correlations [5]. However, control over these systems was limited in the past, as optical lattices have a fixed geometry and cycle times were long due to the necessity of cooling atoms to ultra-cold temperatures. More recently however, optical tweezers have emerged as an alternative [8–10], where each lattice site is generated from an individual laser beam. This allows high control and tunability not only between lattice sites, but also poses the ability to generate arbitrary geometries. As these traps can be made sufficiently deep, this removes the requirement of ultra-cooling atoms, resulting in fast cycle times.

To study manybody effects in these optical tweezers, Rydberg atoms can be employed. They offer the ability of long-range interactions on a micrometer scale [11] and therefore across multiple tweezers. This forms the building blocks for the experiment this thesis is a part of. Hereby, single Potassium-39 atoms are trapped in optical tweezers and excited to Rydberg levels where e.g. blockade effects are measured [12]. The tweezers are generated through

spatial light modulators (SLMs) [13], where arbitrary intensity patterns are formed and projected onto the atomic cloud.

This work presents three new setups towards this experiment. In Chapter 2, loading of atoms from the cloud into tweezers is discussed. The chapter places focus on the theory behind electro-optical modulators (EOMs) which is followed by the characterization of two EOMs, that will be used to improve the loading stage of the experiment and allow deploying more tweezers in the future. Chapter 3 then works towards enabling unity filling in a grid of atoms. For this, a new way of generating the tweezers is introduced in the form of acousto-optical deflectors (AODs), which can move atoms into defects in the lattice. Therefore the theory behind the deflectors is explained and is followed by comparing two algorithms of achieving this sorting of atoms. The chapter is then concluded by describing the driver used for the dynamic tweezers and ways to work around its limitations. Then Chapter 4 presents a spin-selective imaging approach by applying dynamic tweezers that are sensitive to only one spin species using the same AODs as above. The spin-sensitive laser used in this setup was built during this thesis and is concluded with the characterization of this laser.

2. Loading atoms into optical tweezers

In the experiment, SLMs are used to generate two-dimensional arrays of tweezers, which trap single atoms [13]. SLMs allow to generate various geometries, and therefore freely adjustable inter-atomic distances and trapping depths. However, in order to load atoms into the optical tweezers, they have to undergo several cooling stages first. Being vaporized from a solid sample of ^{39}K , the atoms are decelerated by passing through a Zeeman-slower, which cools the atoms longitudinally. The atoms are then trapped, compressed and cooled in a magneto-optical trap (MOT) in the center of the vacuum chamber. The temperature limit in the MOT is the Doppler limit, therefore gray molasses [14] and then a red molasses is used in order to cool even further. When the atoms are cold enough, they are loaded into the SLM tweezers. However, loading directly from the molasses proves difficult, due to the large light shifts of the D2 excited state of Potassium, making it highly anti-trapped. To overcome this issue, trapping and cooling beams can be alternated [15]. By choosing the frequency of alternating the beams much larger than the trapping frequency, the atoms see an effective, averaged trap. Therefore, they don't scatter near-resonant photons, effectively eliminating light shifts.

So far, alternating between molasses cooling and trapping light, called chopping, is implemented using acousto-optical modulators (AOMs). However, the maximum switching speed of an AOM is limited by the speed of sound in the medium (here, TeO_2 has $4.2 \text{ mm } \mu\text{s}^{-1}$) and results in a chopping frequency of 1.4 MHz, governed by the AOM with the slowest rise time, which can be seen in Figure 2.1. By increasing the chopping frequency, the atoms heat less during each trapping cycle. As already mentioned, the atoms only see an averaged trap given by the duty cycle of the trapping beam. Thus, the pulse shape determines how much trapping power the atoms see. Improving therefore the pulse shape leads to more laser power that can be used per tweezer. This in turn means, more tweezers can be deployed, as the average power increases when the pulse shape is more rectangular. Figure 2.1 shows how the pulse shape is limiting the average power during the cooling cycle as well as during trapping.

Achieving larger duty cycles and higher chopping frequencies is possible by using EOMs,

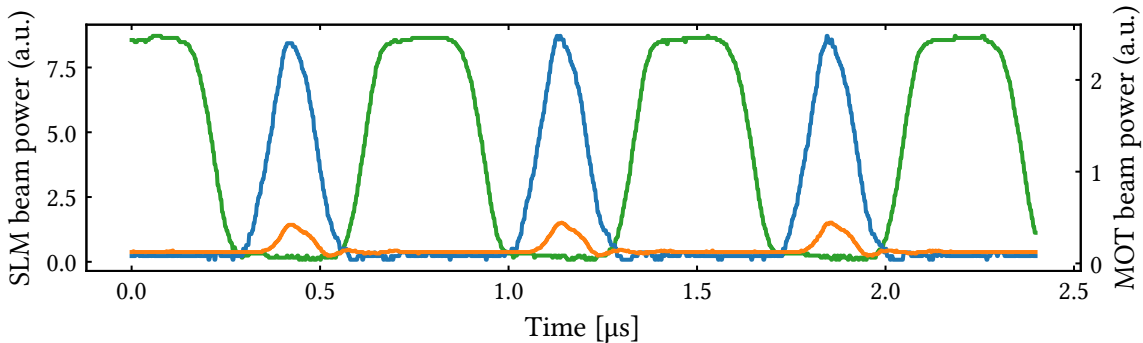


Figure 2.1.: Chopping in the experiment: MOT (cooler (blue), repumper (orange)) and SLM tweezer (green) beams alternate in the chopping sequence. The amplitude of the MOT beams is limited due to the risetime of the AOMs. The scale of the MOT beam amplitudes has been adjusted to match the SLM tweezer scale for better visualization.

which are not limited by acoustic waves. The optical medium is modulated using electric fields, and in fact, can be switched as fast as common condensators [X](#). Light entering the modulator will have its polarization turned, depending on the electric field that is applied. In the following, the polarization of electro-magnetic waves is briefly discussed, which is followed by the main effect governing the devices tested in this thesis – the Pockels effect. The devices are then evaluated by filtering one polarization component and by measuring the intensity of the light after the filter, the rise times and extinction ratio are determined. The new system allows to switch with rise times on the order of nanoseconds, improving the current system by at least two orders of magnitude.

2.1. Theory on Polarization

Switching laser beams using EOMs means turning and filtering the polarization of the light. Therefore in this subsection, the theory behind polarized monochromatic electromagnetic waves, leading to the Pockels effect governing EOMs is discussed.

Polarization of electromagnetic waves is understood as the orientation of the wave in space, transverse to the direction of movement. In general, a wave travelling along the z-axis can be oriented somewhere in the x-y plane. Therefore, writing the electric field component of the light in this basis takes the following form:

$$\mathbf{E}(\mathbf{x}, t) = E_x \cos(kx - wt + \phi_x) \mathbf{e}_x + E_y \cos(ky - wt + \phi_y) \mathbf{e}_y. \quad (2.1)$$

Here, k and w refer to the wave number and frequency respectively. Depending on the amplitudes E_x and E_y and the phases ϕ_x and ϕ_y , the wave can be in different polarization states. If it is not possible to write the wave in this basis, the light is unpolarized. Otherwise, it is **linear**, when either one of the amplitudes E_x or E_y is zero or when the phase difference $\Delta\phi = \phi_x - \phi_y$ evaluates to 0 or π . It is **circular**, when the phase difference $\Delta\phi = \pm\pi/2$ and the amplitudes are the same, $E_x = E_y$. In any other case, the wave is **elliptically** polarized.

Changing the phases of the wave relative to each other gives the ability to influence the polarization. Light traversing a medium will accumulate a phase shift, depending on the refractive index, which affects the speed of light in the medium. Therefore, media that have different refractive indices n_x, n_y along the two axes x and y changes the relative phases of the wave:

$$\phi_x(z) = k_0 n_x z \quad (2.2)$$

$$\phi_y(z) = k_0 n_y z \quad (2.3)$$

where k_0 is the free space wave vector of the light. Then a device that retards the phase difference $\Delta\phi$ by $\pi/2$, which is a quarter of the wavelength, can change linearly polarized light to circularly polarized light (or vice-versa) and is therefore called a $\lambda/4$ waveplate. Similarly, if the phase difference is changed by $\Delta\phi = \pi$, or a half wavelength, then we can turn linear polarization around a given axis or change the orientation of circularly polarized light. This is then called a $\lambda/2$ waveplate. In the experiment, linearly polarized light enters the EOM, which will act as a $\lambda/2$ waveplate, turning the polarization by 90° , making it easy to filter unwanted polarization components and switching the light on and off.

2.2. Electro-optical modulators

Light travelling through a material generally has a speed smaller than the speed of light, given by dividing the speed of light in vacuum by the material-dependent refractive index. Materials can change their refractive index by being exposed to an electric field, which in EOMs is generally a crystal connected to two electrodes. The electro-optical effect discussed in the following is the Pockels effect and applies, when the refractive index changes linearly with the electric field, at which point the EOM is called a Pockels cell. The effect is discussed in the following and the Pockels cells evaluated afterwards.

2.2.1. Pockels effect

As motivated in the previous section, the goal of modulating the light polarization is to change the relative refractive index of a medium in two axes. Following the argumentation from the book Fundamentals of Photonics [16], the Pockels effect can be described by evaluating the refractive index with respect to the electric field applied to the modulator. Writing this as $n(E)$ and applying a Taylor expansion, we get the following expression:

$$n(E) = n_0 + \frac{dn}{dE} E + \mathcal{O}(E^2) \quad (2.4)$$

The Pockels effect is the linear dependence of the refractive index to the electric field, therefore higher orders are neglected. The prefactor dn/dE relates to the change of electric impermeability $\Delta\eta$, which is the ability of a material to be penetrated by an electromagnetic field. From

$$\eta = \frac{1}{n^2}, \quad (2.5)$$

we get

$$\Delta\eta = \frac{d\eta}{dn} \Delta n = -\frac{2}{n_0^3} \frac{dn}{dE} E = \tau E. \quad (2.6)$$

This results in the quantity $\tau = -\frac{2}{n_0^3} \frac{dn}{dE}$, which is called the Pockels coefficient given in units of m V^{-1} . It can be measured by evaluating the refractive index of the material:

$$n(E) = n_0 - \frac{1}{2} \tau n_0^3 E. \quad (2.7)$$

As was seen in Equation 2.2, the refractive index directly affects the phase shift, which in turn changes the polarization of the light wave. Combining the results leads to an equation using parameters typically found in EOMs:

$$\begin{aligned}
 \phi &= k_0 L n \\
 &= k_0 L n_0 - \frac{k_0}{2} L \mathfrak{r} n_0^3 E \\
 &= \phi_0 - \frac{k_0}{2} L \mathfrak{r} n_0^3 E \\
 &= \phi_0 - \frac{\pi}{\lambda_0} L \mathfrak{r} n_0^3 E
 \end{aligned} \tag{2.8}$$

where the relation $k_0 = 2\pi/\lambda_0$ of the wave number was used.

In this application, the Pockels cells act as dynamic wave retarders. Given results from Section 2.1 we can tune the phase difference $\Delta\phi = \phi_x - \phi_y$ along the axes x and y by applying an electric field. With the correct parameters, the phase difference lets the EOM act as a $\lambda/2$ or $\lambda/4$ waveplate. The following relations will help find the main formula governing Pockels cells, resulting in the voltage that needs to be applied to the EOM in order to turn the polarization by a given amount.

By labeling the refractive index in two dimensions as:

$$n_x(E) = n_{0,x} - \frac{1}{2} \mathfrak{r}_x n_{0,x}^3 E \tag{2.9}$$

$$n_y(E) = n_{0,y} - \frac{1}{2} \mathfrak{r}_y n_{0,y}^3 E, \tag{2.10}$$

the phase difference becomes:

$$\Delta\phi = \phi_{0,x} - \phi_{0,y} - \frac{\pi}{\lambda_0} E L \left(\mathfrak{r}_x n_x^3 - \mathfrak{r}_y n_y^3 \right) \tag{2.11}$$

$$\Delta\phi = \Delta\phi_0 - \frac{\pi}{\lambda_0} E L \left(\mathfrak{r}_x n_x^3 - \mathfrak{r}_y n_y^3 \right). \tag{2.12}$$

The next step is to replace the electric field by a voltage that can be applied to the Pockels cell. For this, two electrodes are connected to the electro-optical material, separated by a distance d , giving the electric field as $E = V/d$. This quantity is replaced into Equation 2.14. By realizing that the phase is unitless, all other prefactors of the voltage can be combined into one quantity, called the half-wave voltage V_π :

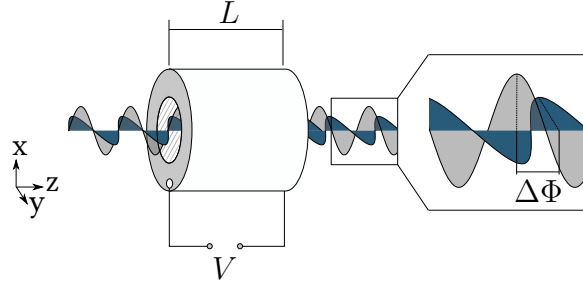


Figure 2.2.: Schematic view of light passing through an EOM with length L . The electrodes are positioned on the front and back side of the modulator, the same faces the light enters and exits. The light exiting the EOM has a relative phase shift $\Delta\Phi$ depending on the change of refractive index due to the applied voltage V .

$$V_\pi = \frac{d}{L} \frac{\lambda_0}{\mathfrak{r}_x n_x^3 - \mathfrak{r}_y n_y^3}. \quad (2.13)$$

Thus, the phase difference can be rewritten as:

$$\Delta\phi = \Delta\phi_0 - \pi \frac{V}{V_\pi}. \quad (2.14)$$

Therefore, applying the voltage V_π , the Pockels cell will act as a $\lambda/2$ waveplate. A visual representation of the modulator and the light passing through it is given in Figure 2.2, highlighting the change in relative phase of the two components of the electro-magnetic wave.

We have seen, how applying a voltage to an electro-optical medium changes the refractive index and therefore affects the phase of an electromagnetic wave. By having two refractive indices in two axes, whose relative change depends on the applied voltage, it is therefore possible to modify the circularity and linearity of the polarization in an electro-optical modulator.

2.2.2. Driving a Pockels cell

With an understanding of the Pockels effect governing the EOMs tested in this thesis, the next step is driving the Pockels cells with the voltages used for switching. As the rise and fall times of the switched Pockels cells are crucial and depend only on the speed of applying

the electric field, it is important to build electronics that can provide these fast rise and fall times. However, materials suitable for use as EOMs, such as β -bariumborate (BBO) and rubidium tanyl phosphate (RTP) have half-wave voltages in the kilovolt-regime, meaning not only does the hardware have to switch on fast timescales, but it also needs to be able to handle high voltages.

The Pockels cell drivers discussed in the following (by BME Bergmann) fulfill these requirements. Moreover, it contains viewports for the laser light, such that the Pockels cell can be integrated into the driver to not expose the high voltage to any parts of the experiment but the modulators. The driver has an input for the high voltage and option for watercooling in order to compensate temperature instabilities on the Pockels cell. Furthermore, it contains four inputs, that allow to have full control over the switching of the voltages. This means, the EOMs can be switched on and off by applying TTL signals to the inputs of the driver.

In order to correctly drive the Pockels cell and therefore turn the polarization of the light, it is necessary to understand the switching logic used inside the driver. Schematically, the driver is divided into the four switches mentioned above, that are controlled from the user: ON A, ON B, OFF A and OFF B. Two switches are connected to either side (labeled A and B) of the Pockels cell, such that A controls one electrode and B the other. Most importantly, the ON X and OFF X (X referring to either A or B) switches work exclusively, so sending a high to ON X also sends a low to OFF X and vice-versa. It is then possible to apply either a positive high voltage or a negative high voltage, depending on the state of the switches. For full identification of the circuit, which is given in Figure 2.3, the side containing the positive voltage information is called high side and similarly the side containing the negative voltage information is called low side. The figure shows switching logics for two different drives used in the experiment. These are named by the manufacturer as dpp-type and bpp-type.

A requirement for our experiment is, to have the EOMs work consistently. This means it is preferable to only apply one type of voltage, because it can not be guaranteed that applying the same voltage with different polarity results in the same shift in polarization. This is due to the high fidelity of the Pockels cell with respect to the input polarization and therefore highly depends on the alignment of the Pockels cell. The diagram in Figure 2.4 shows pulses applied to the switches on the A and B side, necessary to only drive positive voltages to the Pockels cell.

For the bpp-type driver, this is straightforward, as closing high side A and low side B gives a positive voltage across the EOM and the inverse connects ground to ground through the EOM, giving zero voltage. The dpp-type driver on the other hand, has high and low voltages

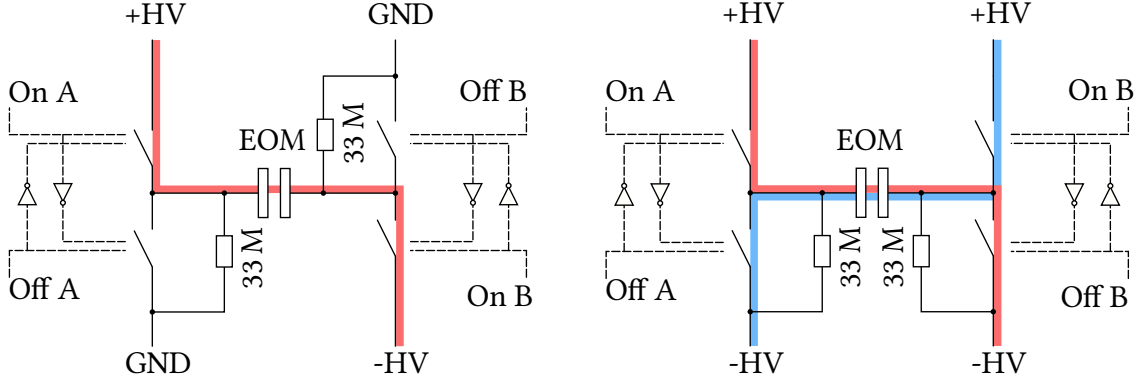


Figure 2.3.: Schematic of the high voltage switches used inside the bpp-type (left) and dpp-type (right) Pockels cell driver from BME Bergmann. Not-Gates on both A and B sides ensure that there is always a potential over the Pockels cell. The blue and red paths indicate the connection to apply a positive and negative voltage over the Pockels cell respectively.

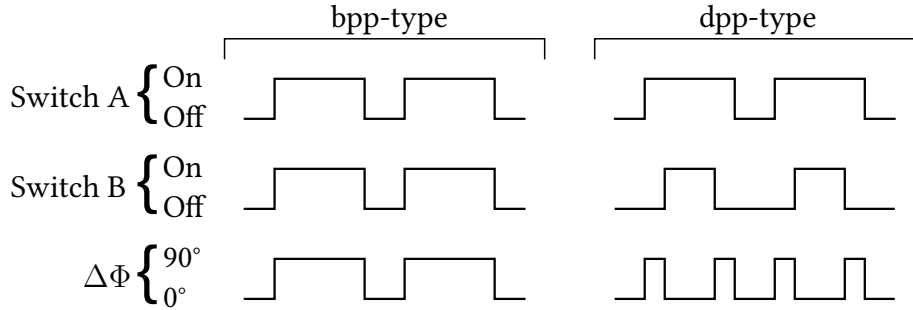


Figure 2.4.: Timing diagrams for the Pockels cell drivers to turn the polarization of the EOM 90°. To get a positive high voltage from the bpp-type driver, the A and B side ON/OFF switches are flipped simultaneously. The dpp-type driver is more flexible, since it also allows negative voltages. The timings displayed here are an example to only apply positive voltages across the Pockels cell.

on either side of the Pockels cell. Therefore, the sequence that results in positive and then no voltage across the EOM is, to close high side A and low side B switch, providing a positive voltage across the EOM. Afterwards, connecting high side A and high side B gives the same voltage on either side of the Pockels cell, resulting in a net zero voltage. After this point, low side B is closed again, providing the same state as before. In the timing diagram, the low side A switch would be closed at this point. It is possible to keep high side A closed the entire time, however it is recommended in the documentation to alternate both switches in order to relax their states.

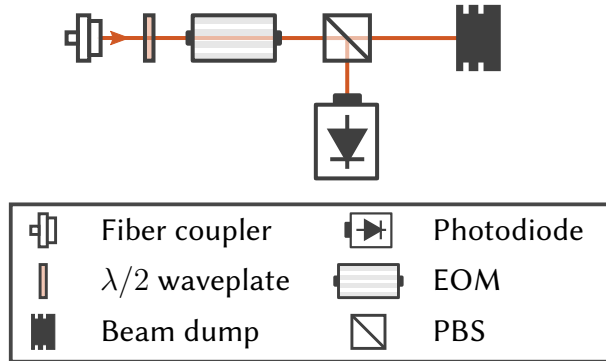


Figure 2.5.: The efficiency of the EOMs were evaluated by setting the polarization of the incoming light either horizontal or vertical using the waveplate. The Pockels cell will then periodically turn the polarization 90°, which can be seen by measuring the voltage on the photodiode.

2.2.3. Testing and evaluating pockels cells

Two pockels cells (from Leysop Ltd.) are characterized in the following. The EOMs in contrast to the AOMs implemented in the current setup allow longer duty cycles of the tweezer light. Switching laser light is achieved in Pockels cells by exploiting the fact, that linearly polarized light can be filtered out. In the following, a polarizing beam splitter (PBS) acts as the filter directly after the modulator as seen in Figure 2.5. This way, the setup can be configured such that applying no voltage means light passes through the beam splitter, while applying V_π means the light gets reflected 90° off the beam splitter, save for a fraction of light, given by the extinction ratio of the beam splitter (typically for the ones used in the experiment, manufactured by Thorlabs, the extinction ratio is about 1000:1).

Two Pockels cells were characterized by placing a photodiode on one end of the beam splitter. The EOMs are labeled by the material of their nonlinear crystal, RTP and BBO. Their characteristics are summarized in Table 2.2.3, where half wave voltages is given for 1064 nm light. Both EOMs are used in the chopping condition discussed earlier, where the RTP crystal will be used for the 770 nm and the BBO for the 1064 nm tweezer light.

First of all, the rise and fall times of the EOMs are determined. Light whose polarization component was filtered through the PBS arrives at the photodiode. For sufficiently high bandwidths on the photodiode and oscilloscope, the flanks of the signal are resolved and the rise time can be evaluated by fitting the function

$$f(x) = \frac{\text{high}}{1 + \exp(-x/\tau)} + \text{low}, \quad (2.15)$$

	RTP	BBO
Aperture (crystal dimensions)	3 mm	3 mm
Total crystal length (2 crystals)	30 mm	50 mm
Approximate half wave voltage (1064nm)	1.0 kV	2.8 kV
Peak damage threshold (1064nm, 1ns pulse)	$> 1 \text{ GW cm}^{-2}$	$> 1 \text{ GW cm}^{-2}$
Insertion loss	< 2 %	< 1.5 %

Table 2.1.: Characteristics of the two Pockels cells with their respective non-linear crystal materials being RTP and BBO given from the datasheet of the manufacturer. The aperture, damage threshold and insertion loss are given for future reference.

where *high* and *low* refer to the high and low level of the signal respectively, which will come in useful later when evaluating the extinction ratio. The signals in Figure 2.6 were recorded for both EOMs, however from the low number of sampled points it is clear, that the oscilloscope used for the measurement is a limiting factor. Moreover, harmonics appear when the signal has risen to the upper level, indicating that the bandwidth of either the photodiode or the oscilloscope is too low. For this measurement, the oscilloscope (Teledyne Lecroy Wafesurfer 510) has a samplerate of 10 GS s^{-1} and a bandwidth of 1 GHz. The photodiode is a home-built model, whose bandwidth has not been evaluated. The fit can't be applied to the data, due to the low number of points, however an upper bound for the rise time can still be given by measuring the distance between the last point on the lower level and the first point on the upper level. For both crystals, this means that the rise time is at least a fraction of a microsecond. In contrast to the AOMs that are currently in use, this is already an improvement by at least one order of magnitude (see Figure 2.1).

However, the manufacturer of the Pockels cell driver has done independent tests on the same EOMs used here. The data is available on their website [17] and they measured rise times for RTP and BBO as 3 ns and 4 ns respectively, which therefore improves on the AOM setup by three orders of magnitude in rise times.

Another important parameter is the extinction ratio, which is the amount of light that is left, when the device is supposed to be off. It is evaluated by the ratio of the *high* to the *low* level of the signal. Figure 2.7 shows signals taken for both crystals using the same setup as before. In order to correctly evaluate both levels, it is necessary to note, that photodiodes are susceptible to dark noise, which is electrical noise falsely registered as light. To compensate

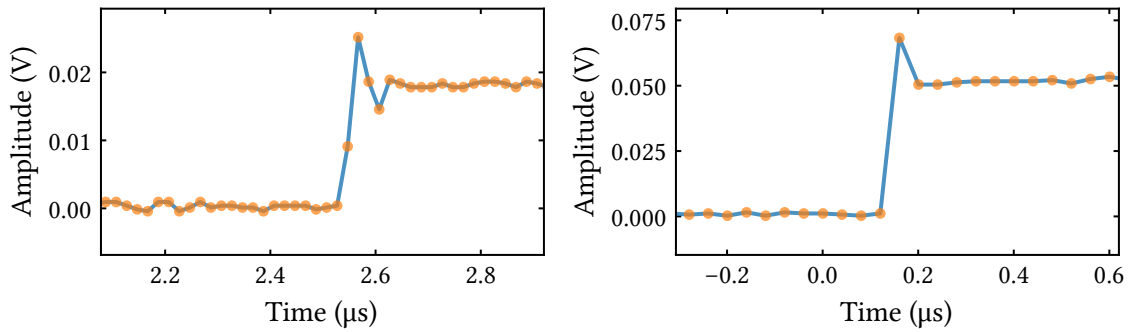


Figure 2.6.: The EOM was turned on, in order to measure rise times. However, the photodiode and oscilloscope both limit the measurement with their bandwidth and sampling rate. However, an approximation to the rise time can be given, by subtracting the last data point on the low level and the first level on the high level, giving at least a fraction of a microsecond for both EOM types.

	<i>upper</i>	σ_{upper}	<i>lower</i>	σ_{lower}	<i>upper/lower</i>
RTP	1.9×10^{-2}	6.2×10^{-4}	3.7×10^{-4}	5.2×10^{-4}	5.1×10^1
BBO	1.9×10^{-2}	8.3×10^{-4}	9.6×10^{-4}	7.4×10^{-4}	5.7×10^1

Table 2.2.: Measuring the extinction ratio requires finding the high and low levels and calculating their ratio. It is noteworthy, that the standard error on the low level is of the order of the mean, therefore the ratio has an infinitely high upper bound.

for this, a dark image was taken, with the laser beam off, and the mean of the dark image was subtracted from the signals used to evaluate the extinction ratio. The high and low levels are then given by selecting points of the respective level after it has stabilized, which are highlighted in Figure 2.7. Giving an upper bound to the extinction proves difficult, as already the standard deviation on the low level for both crystals is on the order of the mean. Nonetheless, relevant parameters for the extinction ratio for both crystals are given in Table 2.2.

However, the lower bound is the fraction of the mean values from the two levels, which for RTP gives 51 : 1 and for BBO 57 : 1. The manufacturer provides an extinction ratio for the RTP crystal of > 200 : 1, however no value is given for BBO. This means, that our measurement is limited by the photodiode and in order to validate the value given by the manufacturer, it is necessary to reduce the dark noise for example by cooling the photodiode or alternatively, using a faster, low noise photodiode.

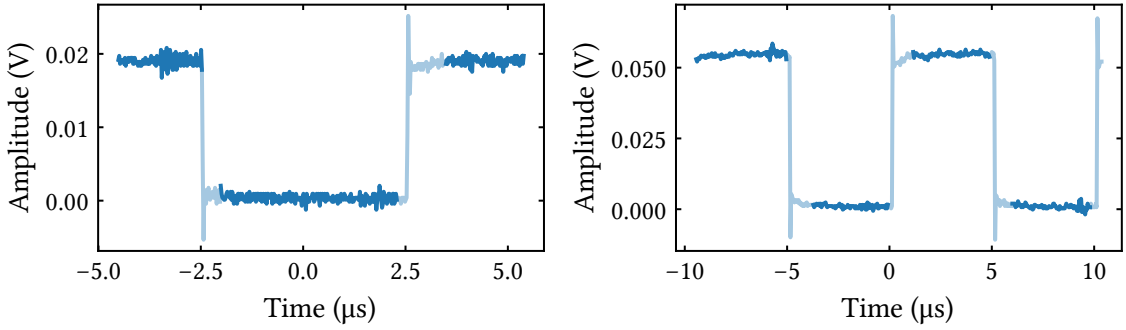


Figure 2.7.: Measurements of extinction ratio for RTP (left) and BBO (right). The highlighted values were used to find the high and low level, by taking their mean. However the uncertainty on the low level is too high to give a fair value on the extinction ratio.

As the chopping frequency in the current experiment is limited to 1.4 MHz, the upper bounds for the repetition rate are also a crucial criterium that needs to be evaluated. The measurement showed an inconsistency, meaning the amplitude of the signal from the Pockels cell changed depending on the repetition rate. This was most notable in the RTP crystal. To quantize this in more detail, a program was written, that ramped the repetition rate up in 60 s intervals, after which the resulting signal was recorded and the amplitude evaluated. This results in the diagram shown in Figure 2.8. However, in contrast to what was said in Section 2.2.2, alternating voltages were applied to the Pockels cell. Measuring the signals showed, that the inconsistent behaviour was worse if only one type of voltage was applied. The diagram clearly shows resonant-like behaviour for RTP. This means, that in the future, the chopping will have to be carried out around 1.5 MHz, where the amplitude of the signal is close to the maximum and therefore loss of laser power is mostly only insertion loss into the EOM.

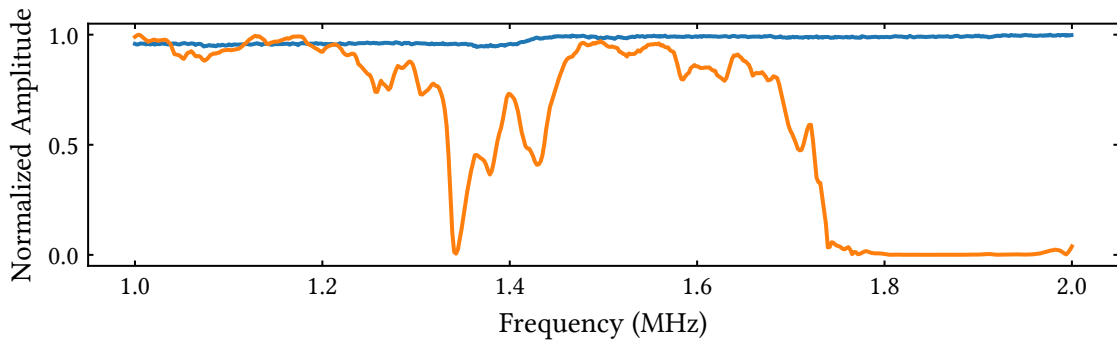


Figure 2.8.: Shown is the amplitude of a laser whose polarization was rotated by a Pockels cell and then filtered using a polarizing beam splitter. The frequency is the repetition rate of the voltage placed into the EOM. The two materials are RTP (orange) BBO (blue). The curves are normalized to their maximum value.

3. Sorting of atoms

Tweezer arrays are especially suitable to study manybody systems, as arbitrary patterns can be configured, which is not possible when using optical lattices. In our experiment, atoms are cooled in optical molasses and loaded into tweezers in a chopping sequence, discussed in Chapter 2. However, in the loading stage, parity projection induces light assisted collisions of the atoms [18], which effectively heat pairs of atoms out of the trap. This leaves only sites occupied, that originally had odd number of atoms, resulting in a total occupation of 50% of atoms across the tweezer array. It is desired to have a fully occupied grid of atoms each run, however post-selection is unfeasible, as even on a 3×3 grid of atoms, the chance of fully occupying the array is only $0.5^9 = 0.2\%$.

Consequently, the solution is to rearrange the atoms of the system, which has demonstrated before [8, 9, 19]. As mentioned, the tweezers in our experiment are generated by SLMs. In order to rearrange the atoms however, they need to be transferred from the static SLM tweezers, into new dynamic acousto-optically deflected tweezers. These move the atoms adiabatically to new positions, while keeping the others stationary. In this way, atoms are moved along pre-calculated paths to fill gaps of the pattern. The following chapter discusses the sorting of atoms by using AODs as the device of choice for programmatically deflecting a laser beam. Using this device, it is also possible to generate an array of tweezers, so that multiple sites at the same time can be moved.

3.1. Acousto-optically deflected tweezers

Being able to quickly change the position of a laser beam is the most fundamental prerequisite of sorting atoms. The process has to happen on short timescales compared to the lifetime of atoms and with high accuracy. As AODs can fulfill this requirement, the process of light deflecting off a sound modulated crystal is discussed in the following. By applying sound waves, it is possible to move a laser beam or split it into multiple beams. The optical element handling the deflection is called an AOD and works very similar to an AOM.

However, in an AOD, the first deflected order is stronger and higher orders are generally not visible.

After going through the theory of acousto-optical deflection, the AODs in question are described, following the setup of generating the tweezers needed for the rearrangement of the atoms.

3.1.1. Acousto-optical effect

The acousto-optical effect describes the way optical waves deflect off sound waves in a solid medium, which is generally a crystal. This means, sound waves propagating the crystal modulate the positions of the atoms in the lattice, which in turn affects the refractive index on a macroscopic scale. If the sound wave is a planar wave, then the modulated refractive index is written as a function of position x and time t [16]:

$$n(x, t) = n - \Delta n_0 \cos(\Omega t - qx). \quad (3.1)$$

In this case, the offset n is the refractive index in absence of sound waves. Moreover, Δn_0 , is the amplitude, Ω the frequency and q the wavenumber given by the sound wave.

Using this relation, the next step is calculating the deflection angle off the medium. In the following, a short summary is given, the detailed analysis can be found in [16]. Starting from the assumption that the incident optical wave has a much higher frequency than the sound wave, then the light entering the medium sees the sound waves as stationary and the medium's crystalline shape is given by the sound wave.

Then the description of light passing through a medium is given by the Bragg condition, and is used to calculate how light is partially reflected when leaving the medium. In order to calculate this quantity, the medium is broken up into slices, off which the optical wave partly reflects, given by the Bragg diffraction. Each slice has a partial reflectance amplitude Δr , depending on the refractive index n and the angle of the incident optical beam with respect to the medium. The total reflectance amplitude r can then be calculated by integrating over all slices and carries over the dependence on the angle. By maximizing this relation, the angle resulting in the maximum reflectance amplitude is given by the Bragg condition:

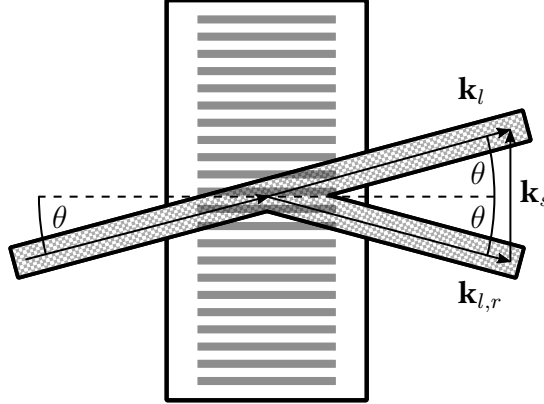


Figure 3.1.: Schematic operation of an AOD. Light waves travelling in direction \mathbf{k}_l are deflected off the sound waves with direction \mathbf{k}_s , resulting in a reflected beam $\mathbf{k}_{l,r}$. The optical waves are deflected under the Bragg condition, which can be calculated via the vector relation $\mathbf{k}_{l,r} = \mathbf{k}_l + \mathbf{k}_s$.

$$\sin \theta = \frac{\lambda_l}{2\lambda_s}, \quad (3.2)$$

where λ_l and λ_s refer to the wavelength of the light and sound waves respectively.

The maximum of the reflectance amplitude with respect to the angle is very sharp, such that there is a deflected beam only if the angle between the wave vectors of the optical wave \mathbf{k}_l and the sound wave \mathbf{k}_s matches the Bragg condition. Thus, another way to arrive at the Bragg condition is by calculating the trigonometric relation in Figure 3.1. With

$$|\mathbf{k}_l| = |\mathbf{k}_{l,r}| = \frac{2\pi}{\lambda_l} \quad (3.3)$$

$$|\mathbf{k}_s| = \frac{2\pi}{\lambda_s}, \quad (3.4)$$

it follows directly, that

$$\sin \theta = \frac{|\mathbf{k}_s|/2}{|\mathbf{k}_{l,r}|} = \frac{\lambda_l}{2\lambda_s}. \quad (3.5)$$

Using the acousto-optical effect in order to modify tweezer positions, it is necessary to break the dependence of the angle between incoming optical wave and acoustic wave, while keeping the dependence on the angle of the outgoing light. This is achieved by modelling

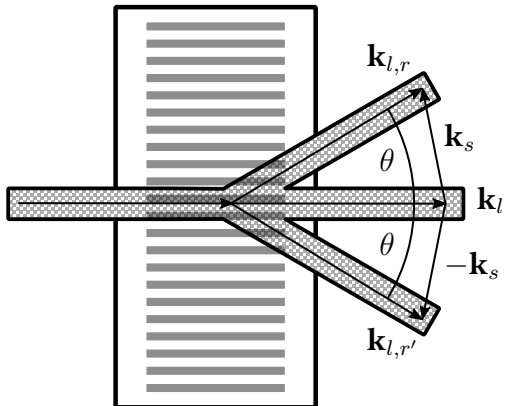


Figure 3.2.: Similar to Figure 3.1, light is deflected off sound waves in an acousto-optical medium. This time, the sound wave is modelled as a Gaussian distribution of planar waves, such that besides the transmitted component, two more orders are deflected.

the sound wave as a Gaussian distribution of planar waves, travelling radially outwards from the origin of the sound. As a consequence of this, it will always be possible to fulfill the Bragg condition, no matter how the light enters the medium.

In Figure 3.2, an optical beam enters a medium straight and exits on a diffracted angle $\pm\theta$, given by the Bragg condition. Using again the trigonometric relations from Equation 3.5, there are now additional acoustic waves travelling in opposing directions, where the optical and sound wave meet. In the approximation of small angles, the Bragg condition then simplifies to:

$$\theta_{\pm} \approx \sin \theta_{\pm} = \pm \frac{\lambda_l}{\lambda_s} = \pm \frac{f_s}{v} \lambda_l, \quad (3.6)$$

where the speed of light in the medium v needs to be taken into account.

This means, that the angle of the first deflected orders from the AOD only depend on the wavelengths of the light wave λ_l and the sound wave λ_s . In other terms, the angle of deflection can be tuned by changing the wavelength of the sound wave. As the deflector is driving with an RF-generator, we generally speak of the frequency and not the wavelength of the sound wave. Using the deflector for sorting, means taking first deflected order and blocking the others. This way, a beam can be moved by driving a frequency ramp on the sound wave, thus changing the angle of the first deflected order. Consequently, the change of angle depending on the change in frequency of the sound wave is interesting and is then calculated as:

$$\Delta\theta_{\pm} = \pm \frac{\Delta f_s}{v} \lambda_l \quad (3.7)$$

Thus, all parameters required for manipulating the position of laser beam have been calculated, such that the tweezers can be operated for resorting. We have seen how optical light is deflected off sound waves in media and how this can be used to re-position laser beams and in the long run, move atoms along paths. There are generally two types of AODs available, that are normal mode and shear mode. In a normal mode AOM, the shape of the crystal viewed from the top, is rectangular, while in a shear mode, the crystal's front and back sides are cut at an angle. This means, sound waves won't be Gaussian anymore, but instead be shear waves, meaning their velocity is slower. This is in general preferable, as we made the assumption, that the speed of the sound wave is much slower than the speed of the light wave, and thus this condition is reinforced. All in all, after having understood the operation of AODs, the following chapter explains the setup in place for sorting the atoms.

3.1.2. Preparation of the tweezers beams

With the derivations from the previous chapter, it is possible to calculate the position of the laser beam, depending on the frequency of the sound wave propagating the AOD. However, the beam has to be prepared before entering the deflector, meaning its polarization has to be adjusted. After the deflector, the beam will pass an objective into the vacuum chamber and therefore needs to be shaped correctly before the objective. The setup of the laser, as well as the configuration of AODs, in order to sort in two dimensions, is described in the following.

The deflectors ((AA DTSXY-400-800.860) from Pegasus optics) and their characteristics are given in Table 3.1.2. The AODs are driven by RF-frequencies, which map 1:1 to the frequency of the sound wave. In order to deflect in two dimensions, two deflectors are placed in series, which are turned by 90° with respect to each other. This way, the first order on the first AOD will extend e.g. into the x-axis, while the first order of the second AOD will then extend along the y-axis. Together, exiting the deflectors will be a 2×2 grid of laser beams, which can be seen in Figure 3.3. These are the $(x = 0, y = 0)$, $(1, 0)$, $(0, 1)$ and $(1, 1)$ orders, however, only the $(1, 1)$ order will be used, as this is the one that is deflected based on the sound wave placed into the AOD.

Central drive frequency at 795 nm	(102 ± 4) MHz
Bandwidth	36 MHz
Max optical power density	5 W mm^{-2}
Max RF power	2 W
Laser beam diameter [D]	$500 \mu\text{m} < D < 6 \text{ mm}$
Material (speed of sound)	TeO ₂ (650 m s^{-1})
Scan angle	$(44 \text{ mrad})^2$

Table 3.1.: Properties of AA DTSXY-400–800.860 crossed AODs from Pegasus optics.

The details of the configuration and characterization of the devices used in the experiment are given in [13]. The crossed AODs configuration described above is used in the following for rearranging the atoms. Additionally, the dynamic tweezers generated from the deflectors are also used for a spin-selective imaging approach, which is further described in Chapter 4. This means, beam paths of two different lasers are passing through the same deflectors. In Figure 3.4, the setup including both laser beams is shown. The first laser, used for the characterization in [13] and later sorting of atoms, as well as for testing reasons regarding the tweezers in the following and has a wavelength of 795 nm. The spin-selective laser has a wavelength of 768 nm and is further discussed in Chapter 4.

The first step in the setup, is stabilizing the intensity of laser beams, by measuring their power on a photodiode and using proportional-integral controllers to adjust the signal. They then pass a $\lambda/2$ waveplate to adjust the polarization, which affects the efficiency of the AOD. The deflectors, which are connected to RF-synthesizers, then produce the 2×2 grid of laser beams. Afterwards, a $f = 75 \text{ mm}$ lens, projecting the center of the AOD-array, extends the beam spatially until it is collimated using a $f = 1000 \text{ mm}$ lens. This sets the correct beam size for the objective to project the beam onto the atoms.

3.1.3. Moving tweezers

It was shown, how the position of the laser is calculated using the Bragg condition in Equation 3.1.1. With the laser setup in place, the question remains how the change of the sound wave frequency affects the position of the tweezer in the plane of the atoms. This is calculated, by taking into account the magnification M due to the telescope created between the $f = 1000 \text{ mm}$ lens and the objective, having an effective focal length of 33.18 mm. From the point of view of the atoms, this results in $M = \frac{1000}{33.18} = 30.14$, meaning the distance

between the atoms Δx is magnified by this amount. Continuing from the atom's reference frame, their magnified distance is then given on the $f = 75 \text{ mm}$ lens as a distance $\Delta x_{magnified} = Mx$, which projects the position into the center of the crossed AOD configuration at an angle $\tan \theta \approx \theta = \Delta x_{magnified}/75 \text{ mm}$. With Equation 3.1.1, this results in a change of frequency on the AOD:

$$\Delta f = \frac{\Delta x_{magnified}}{75 \text{ mm}} \frac{v}{\lambda}, \quad (3.8)$$

given an optical laser wavelength of λ . The speed of sound for the AODs, which is the speed of sound in TeO_2 is $v = 650 \text{ m s}^{-1}$. This means a typical atomic distance of $10 \mu\text{m}$, requires a change in frequency of $\Delta f = 3.3 \text{ kHz}$.

3.1.4. Tweezer homogeneity

With all the building blocks in place, for driving acousto-optically deflected tweezers, they are now ready to be imaged and tested. The beam path shown in Figure 3.4 was used, except the objective at the very end was replaced by an $f = 500 \text{ mm}$ lens and a camera (XIMEA MD028MU-SY). This way, the tweezers are visible directly on the camera. Moreover, in order to measure the homogeneity more accurately, part of the beam is split and coupled into a photodiode after the $f = 500 \text{ mm}$ lens. This way, an image was taken with a camera and at the same time, a trace was taken from the signal of the photodiode. Although it is technically possible, to draw a grid with the AODs, by applying a superposition of multiple frequencies, the measurement discussed in the following was taken by turning on each tweezer separately one after another. This way, they can be distinguished powerwise.

The Figures 3.5 and 3.6 show the results of these measurements. It can be seen in the camera image, that there is a slight field of view effect in the top-left corner. The order of activation of the tweezers was to start in the lower right hand corner, continuing to the left and after row-wise towards the top. This allows to map them back to the intensity seen in the oscilloscope picture. The oscilloscope also shows an intensity ramp towards the end, which suggests the same field of view and therefore being an effect of the beam not perfectly aligned. Nonetheless, the intensity difference between the first and last set of tweezers is about 0.1 V or 5% when the distance between lattice points was given by a frequency difference 1 MHz . However, as noted in Section 3.1.3, this is higher by almost a factor of 1000, suggesting that the tweezer homogeneity will be much higher once integrated into the experiment.

3.2. Sorting algorithms

With the laser now passing through the crossed AODs and being shaped for the objective, it is time to rearrange the atoms for the experiment. Doing so requires the knowledge about unloaded SLM tweezers, which is achieved by imaging the atoms and evaluating their positions. Of course, atoms can't be lost during imaging, therefore cooling and trapping beams are chopped together and the scattered light from the cooling beam is recorded as a fluorescence image. From then on, atoms need to be moved along paths in order to fill the gaps. They can be lost, if the move is on the order of the scattering rate, as then the trap moves out of range while an atom is in the excited state. Generally speaking, the move needs to be as fast as possible, since heating effects discussed in Chapter 2 lead in our experiment to $1/e$ lifetimes on the order of 80 seconds. Therefore, already 1.2% of atoms, or at least one atom in a 10×10 grid are lost after one second.

Sorting the atoms as fast as possible in order to reach 100% filling requires paths that minimize the total sorting time. An obvious choice here is Dijkstra's algorithm, which is designed to find the minimal path between two points, in an arbitrary landscape. However, since the paths have to be calculated while the atoms are loaded, this means computation complexity has to be taken into account as well. Since Dijkstra's algorithm scales with $\mathcal{O}(n^4)$ , where n is the number of atoms, this can lead to long computation times. However, some simplifications can be made, which can help come up with an algorithm that is both fast in calculation speed, as well as having fast sorting speeds. For one, we are operating on a rectangular grid and thus make the simplification to only move vertically or horizontally and not diagonally. Secondly, atoms that have started moving, stay in the tweezer until they arrive at their destination, and thus the tweezer does not suddenly jump to a new target. This is a sensible simplification, as an atom has to be transferred from the initial tweezer array to the moving tweezers (and back again when it arrives at the destination), which also takes up time. In the description of the algorithms, the grid is separated into a target and a reservoir region. This means we are trying to get a 100% filling in the target region, by moving atoms out of the reservoir region. Any atoms left in the reservoir after the sorting is finished, will be discarded. On the other hand, while there are still holes in the target region, the algorithm will look for ways to fill the gaps using atoms from the reservoir region.

Two algorithms (pathfinding and compression) are presented in the following, one is based on solving a pathfinding problem and moves one atom at a time. The other uses the feature of the AOD, that allows to work move several tweezers at once, by applying multiple RF frequencies, in order find a more parallelized approach.

ref

3.2.1. Pathfinding

The pathfinding problem is solving the problem of finding the shortest path between two points. For sorting of atoms, this means identifying the shortest set of movements to relocate an atom from the reservoir region to an empty spot in the target region. The algorithm described in the following was developed by Jan Werkmann¹ and is discussed in [20]. With the simplifications of above, atoms only move either horizontally or vertically. The algorithm will then identify a path that first moves the full distance of the one dimension, then the full distance in the other, at which point the atom has arrived at its destination. This is a sensible approach, as only one frequency ramp per dimension is driven, but does not change the total distance moved, since the atom won't move on diagonals. Then there are only two possible paths every atom can take, either going first vertically then horizontally, or the other way around. The optimal path is then the one with the least amount of atoms in it. If there happens to be an atom in the path, the algorithm segmentizes the path, moving the obstacle atom along the path into the unoccupied spot, with the other atom following after. An example path is shown in Figure 3.7.

3.2.2. Compression

As was just discussed, the pathfinding algorithm moves atoms one by one. However, one might want to find a way to parallelize sorting, therefore decreasing the sorting time. By supplying an AOD with multiple RF-frequencies, it is possible to create multiple movable tweezers. The compression algorithm discussed here makes use of this in order to reduce the total time of the sorting, as well as having a lower computation time with respect to the pathfinding algorithm.

The compression algorithm works by picking a full line of atoms. It then moves the selected atoms along the line towards the target area, grid point by grid point. If an atom would collide with an obstacle, that is, either another atom not currently inside an AOD tweezer, or the end of the target area, then that atom is transferred back to the SLM tweezer grid, and not moved in the next step. This process is shown in 3.8. When one line is finished moving according to this end condition, the next line is picked up and the process repeated. This is done first for all rows, then for all columns, and finally, all atoms are found in one corner of the grid. Doing it this way, effectively compresses all atoms in the grid into an area.

¹<https://github.com/PhyNerd/GridRouting>

Due to the nature of the algorithm, there can still be holes in the target area when the sequence is finished. To overcome this problem, following the compression stage, the pathfinding algorithm will fill the final few gaps, whose runtime is favorable towards low hole numbers.

To further take advantage of the compression algorithm, a geometry is chosen, which has the target area in the center of the grid and the reservoir surrounding it, as seen in Figure 3.8. As the algorithm pushes the atoms into a corner, the grid can simply be split up into four sections. Then the moves for each section is individually calculated. Ending up with moves in the row-dimension and moves in the column-dimension for each section, they can then be merged together, if they operate on the same line, which is illustrated in Figure 3.9. As such, the sorting time of moving atoms into one corner is effectively the same as moving the atoms into the central area, by splitting it up into sections and merging the steps.

3.2.3. Comparison of the two algorithms

As the pathfinding and compression algorithm are both solving the same sorting problem, it is necessary to make a performance comparison between the two. For the simulation of the performance comparison, the target area was chosen to be in the center, surrounded by the reservoir region. This gives a geometry, which has holes as close as possible to reservoir atoms, therefore giving a minimal number of movements for the pathfinding algorithm, while also making use of the performance gain that was highlighted in Section 3.2.2 for the compression.

Relevant parameters that need to be compared, are the sorting and computation time, as they need to be much slower than the lifetime of the atoms. Atom loss can also occur, whenever the atoms are transferred from the SLM tweezer grid to the AOD tweezer grid used for the sorting. This way, the number of transfers are also shown in the following. Simulations were performed, by populating the full grid with atoms with 50 % probability of occupying a grid point. Then each algorithm was run and relevant parameters recorded. Simulations were run for various grid sizes, while trying to keep the fraction of number of atoms in the target area N_{target} to the number of atoms in the reservoir area $N_{reservoir}$ around $\frac{N_{target}}{N_{reservoir}} \approx 0.65$. This has to be compromised for low grid sizes, as the integer nature of grid points only allows natural numbers for reservoir sizes.

The results in Figure 3.10 show that the compression algorithm has a faster sorting and computation time, but has to transfer more atoms into the AOD tweezer grid. However, it also shows that it scales better for increasing grid sizes. A polynomial fit is shown for the

second half of the points, where the rounding issue is less present. The fit parameters are given in Table 3.2.3, from where it can be seen, that the compression algorithm scales more linearly than the pathfinding algorithm.

Pathfinding		
	m	a (ms)
Resorting time	$1.3 \pm 1.7 \times 10^{-2}$	$5.8 \times 10^{-2} \pm 8.8 \times 10^{-3}$
Computation time	$1.8 \pm 8.9 \times 10^{-3}$	$4.8 \times 10^{-5} \pm 3.8 \times 10^{-6}$
Number of transfers	$1.4 \pm 1.8 \times 10^{-2}$	$5.7 \times 10^{-2} \pm 9.2 \times 10^{-3}$

Compression		
	m	a (ms)
Resorting time	$9.7 \times 10^{-1} \pm 1.7 \times 10^{-2}$	$3.6 \times 10^{-1} \pm 5.3 \times 10^{-2}$
Computation time	$1.6 \pm 3.1 \times 10^{-2}$	$9.0 \times 10^{-5} \pm 2.5 \times 10^{-5}$
Number of transfers	$9.5 \times 10^{-1} \pm 1.2 \times 10^{-2}$	$8.3 \times 10^{-1} \pm 8.6 \times 10^{-2}$

Table 3.2.: Comparison of scaling of the two sorting algorithms. For each quantity given in the left-most column, a polynomial $f(x) = aN^m$ was fitted to the points shown in Figure 3.10. This gives m as the scaling and the parameter of interest, resulting in better scaling in every aspect for the compression algorithm.

3.3. Driving an RF-synthesizer for arbitrary pattern generation

One of the most powerful aspects about AODs is the fact, that a superposition of sound waves results in a superposition of light waves in the output. This way, it is possible to generate a grid of tweezers, by supplying each AOD with one or more RF-frequencies. There are a multitude of ways to generate RF-frequencies, one way is using voltage controlled oscillators (VCOs), which can be simple LC-circuits. Using these, it is also possible to drive frequency ramps, however it is not possible to synthesize multiple frequencies from one VCO, meaning it is necessary to use multiple VCOs together. Therefore using this ap-

Maximum sampling rate	1.25 GS s^{-1}
Output level (at max sampling rate)	$\pm 4 \text{ V}$
Transfer speed PC to card	2.8 GB s^{-1}
Memory	4 GB

Table 3.3.: Relevant parameters of the Spectrum M4i.6600-x8 card from the specifications given by the manufacturer.

proach it is possible to sort the atoms one-by-one, however it is not possible to generate grid patterns.

To overcome this issue, we implement a digitizer card (M4i.6600-x8, Spectrum Instrumentation), whose specifications are summarized in Table 3.3.1. Doing so allows to sample arbitrary signals, for example sines, rectangles or even non-periodic ones. A digital-to-analog converter (DAC) on the board converts the sampled points into an analog signal, which can be passed into the AOD.

3.3.1. Functionality of the Spectrum driver

Communication with the card is provided through a low-level interface from the official drivers over a PCIe slot. In the following, two replay modes of the spectrum card are discussed, which are standard replay mode and sequence replay mode. In single replay mode, a signal is sent onto the card, which is played back a set number of times, from start to finish. The sequence replay mode allows to upload sequences during initialization. It is then possible to play any arbitrary combination of the sequences one after another.

The functionality of the card depends on two factors: The layout of the memory, and the readout speed (the sampling rate) of the memory. In the following implementation, two output channels of the spectrum card are used. Doing so, the memory is formatted, such that two bytes of channel 1 data are followed by two bytes of channel 2 data as seen in Figure 3.11. Transferring data onto the memory then requires to fill a buffer, that is, memory on the computer running the driver, that has the same layout as the spectrum card's memory.

With this information, the structure of a program driving the digitizer card follows the format given in Table 3.3.1.

Single replay mode	
Initialization phase	<ul style="list-style-type: none"> • Set sampling rate • Set replay mode to single replay mode • Allocate the buffer memory
Main loop	<ul style="list-style-type: none"> • Sample datapoints of the signal to play and move into the buffer • Transfer datapoints from the buffer to the card • Replay signal N times
Sequence replay mode	
Initialization phase	<ul style="list-style-type: none"> • Set sampling rate • Set replay mode to sequence replay mode • Sample signals to use in the sequence programmed later • Transfer signals onto the card • Allocate the buffer memory (will contain information about the sequence)
Main loop	<ul style="list-style-type: none"> • Fill buffer with information about which signals to play • Transfer buffer to the card • Play sequence

Table 3.4.: Difference in programming when using either the single replay or the sequence replay mode of the Spectrum M4i card. In this case, it is instructive to see, that the single replay mode has an overhead during the main loop compared to the sequence replay mode, which has all sequences stored in memory already.

The maximum transfer speed for transferring data from the PC to the spectrum card is 2.8 GB s^{-1} , this means that it will always be preferable to move as few data as possible. Consequently, if possible, it is advantageous to use the sequence replay mode, as here, almost all data is already transferred in the initialization phase. All that is left to transfer, is the sequence the data pointer is following.

3.3.2. Limits of using the card in the experiment

There are some considerations to make when using a digitizer card as a driver for acousto-optical tweezers. Since the digitizer replays sampled data points from waveforms, this means data points need to be transferred from a computer memory to the digitizer card. The transfer time should of course be kept minimal, since the information about which waveforms to sample is only available when atoms are already loaded into tweezers and their lifetime in the tweezer traps is finite (on the order of 80 s for our experiment). Transferring data points to the spectrum card can be done in advance in the sequence replay mode, however this requires the internal memory of the digitizer to be big enough to hold all possible waveforms to be replayed. Both the transfer time and memory usage are calculated in the following, considering both the standard replay mode and the sequence replay mode.

In order to calculate the transfer time and memory usage, some assumptions need to be made. The assumptions and all necessary variables are summarized in Table 3.3.2. First of all, the central frequency of the AOD is approximately $f_{AOD} = 100 \text{ MHz}$. Therefore, in order to sample a sine at this frequency with at least 10 points per oscillation, means a sampling rate of at least 1 GS s^{-1} . For the M4i digitizer card, this means the next available setting is 1.25 GS s^{-1} and gives about 13 samples per oscillation. Being able to resolve the signal clearly, has the advantage to generate the frequency more accurately, therefore the 10 samples per oscillation is a good limit.

Now in order to calculate the time to transfer an atom adiabatically from the SLM tweezer grid into the AOD tweezer grid (and back again), the relation $\dot{w} > w^2$ needs to be fulfilled, where w is the trap frequency in transverse direction. The following argumentation follows the directions in [21]. In our case, this is on the order of 20 kHz and is fulfilled for a transfer time of $t_{transfer} = 1 \text{ ms}$. In order to calculate the moving time t_{move} for an atom from one grid point to another, the shape of the trap is considered. If the atom is accelerated in the first half of the movement, and decelerated in the second half of the movement, the total distance to transfer the atom is given as $L = at_{move}^2$. The maximal acceleration is found from the trap waist $w = 1 \mu\text{m}$ and its radial frequency $f_{rad} = 100 \text{ kHz}$, as $a_{\max} \approx wf_{rad}^2 =$

Variable	Used or assumed value
Sampling rate	1.25 GHz
Central AOD driving frequency	100 MHz
Adiabatic transfer time to new grid	1 ms
Adiabatic movement time to next grid point	1 ms
Grid size	10×10
Number of tweezer transfers for sorting	60
Number of movements for sorting	40

Table 3.5.: Variables and assumptions used in the calculations for estimation of data transfer time and memory usage under the consideration of the experiment discussed in this thesis.

10^4 m s^{-2} . Therefore, choosing a conservative acceleration $a = 10 \text{ m s}^{-2}$ results in a moving time $t_{move} = 1 \text{ ms}$ over a distance $L = 10 \mu\text{m}$.

With the transfer time, moving time, and sampling rate in place, the size of one signal, in order to move and transfer an atom, can be calculated as:

$$n_{points} = St = 1.25 \text{ GS s}^{-1} * 1 \text{ ms} = 1.25 \times 10^6 \quad (3.9)$$

$$M_{sig} = 2 \text{ B} * n_{points} = 2.5 \text{ MB}, \quad (3.10)$$

where 1 B is one byte and $t = T_{move} = t_{transfer}$. From the simulations of the algorithms in Figure 3.10, we see that assuming a 10×10 grid, there are about 60 tweezer transfers and 40 movements for one sorting. This means 100 sequences need to be played per channel, which is $n_{seq} = 200$ in total. Lastly, the memory for all signals needs to be aligned to a power of two. Therefore, from the transfer speed $v_{transfer}$ in Table 3.3.1 follows the time it takes for one transfer $t_{transfer}$:

$$t_{transfer} = \lceil n_{seq} M_{sig} \rceil_2 v_{transfer} = 183 \text{ ms}, \quad (3.11)$$

where the symbol $\lceil \dots \rceil_2$ refers to rounding up to the next power of two. These calculations set the limit for the single replay mode, however, in the sequence replay mode, the limiting

factor is the memory it takes to store all possible sequences. The storage of the sequences already assumes knowledge of the composition of both channels. Therefore it is necessary to upload every relevant combination of signals for both channels. Working again with a 10×10 grid of atoms, all relevant signals are found from the following table:

Signals on channel 1	Signals on channel 2	Usage
10 intensity ramps up	10 intensity ramps up	Transfer into AOD grid
10 intensity ramps down	10 intensity ramps down	Transfer out of AOD grid
9 frequency ramps up	10 constant frequencies	Move along x-axis
9 frequency ramps down	10 constant frequencies	Move along x-axis
10 constant frequencies	9 frequency ramps up	Move along y-axis
10 constant frequencies	9 frequency ramps down	Move along y-axis

Therefore, by multiplying the signals in the columns and then adding the rows, there are 560 combinations and $n_{seq} = 560 * 2 = 1120$ signals to upload onto the card. Each having a size of $M_{sig} = 2.5$ MB results in a required memory of $M_{req} = 2.8$ GB. More generally, on a $N \times M$ grid, the number of sequences can be calculated via

$$n_{seq} = 2NM + 2N(M - 1) + 2(N - 1)M \quad (3.12)$$

and therefore the required memory is

$$M_{req} = 5 \text{ MB} * n_{seq}. \quad (3.13)$$

With the calculations above, it is possible to apply the pathfinding sorting algorithm to the atoms in a timely manner. However for the compression algorithm, a much larger amount of signals needs to be sampled to cover all possible combinations. Considering, that two sides of the target area are sorting at the same time, and that slices of one row (or column) is selected at the same time, the number of sequences, in one channel, to move one row is then given by

$$n_{seq, row} = \left(\sum_{N=1}^{M-1} N \right)^2 = \frac{1}{4}(M^2 - M)^2. \quad (3.14)$$

The square comes from the fact, that for every frequency ramp on one side, a frequency ramp on the other side of the target area needs to be matched. A similar relation (replacing M by N) is found for the number of sequences for the columns. Then, considering that the channels aren't independent, the total number of sequences is found by:

$$n_{seq} = M n_{seq,col} + N n_{seq,row}. \quad (3.15)$$

Taking also into account, that after the compression phase follows a pathfinding phase, it is already easy to see, that the memory requirement would greatly exceed the available memory of 4 GB on the spectrum M4i on a 10×10 grid.

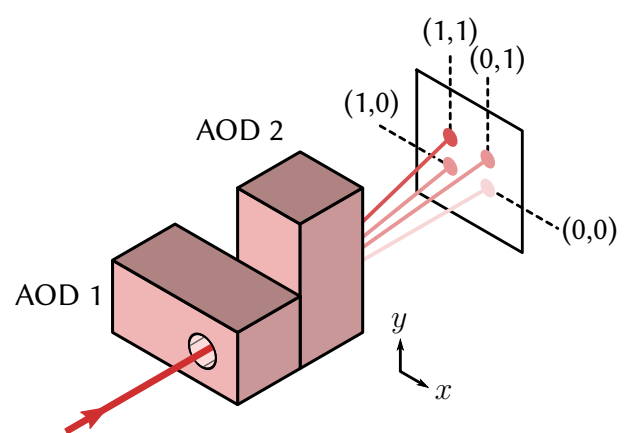
This means, in order to use the compression algorithm, the sequences need to be sampled on-the-fly. This is in general slow, compared to the sorting time. However, it is possible to use parallelization of graphics processing units (GPUs). On a NVIDIA GeForce GTX 1080 Ti, 3584 cores are available, which can all sample part of a signal individually. This means for a sequence of 5 MB, 2 B per datapoint, about 700 calculations are made in parallel. Assuming only rectangles are sampled, this gives one comparison per sampled value and one insertion (into an array). At a clock speed of 1480 MHz [22], results in 0.5 μ s computation time, meaning only transfer speed from the GPU to the digitizer card is relevant. The transfer speed is then given from Table 3.3.1, adding 1.8 ms per move of one row (or column) of atoms.

Since one channel always has a fixed frequency, it is possible to use a VCO for this channel, meaning only half of the signals need to be sampled.

3.4. Conclusion

It was shown how crossed AODs are used, in order to generate movable tweezers. As loading of atoms can only guarantee 50% filling, the tweezers are then used to sort atoms into the gaps, in order to guarantee a perfectly occupied grid, as long as the sorting happens faster than the lifetime of the atoms. Two different algorithms were discussed that move the atoms to their new locations, which are a pathfinding algorithm, moving single atoms and a compression algorithm, which is able to use parallelization, such that multiple atoms are moved at the same time. It was shown that this approach reduces computation time of paths and sorting time of the atoms. Lastly, it was explained how the signals are generated

using a digitizer card and the memory requirement for both algorithms were stated. It was shown, that as long as the grid is small enough, the pathfinding algorithm can be used with the digitizer card, as it has a smaller memory footprint. However, for a grid size of 12×12 already, the memory of the digitizer card (Spectrum M4i.6680-x8) is not sufficient, such that on-the-fly calculations are inevitable and the compression algorithm, with smaller computation time, can be used.



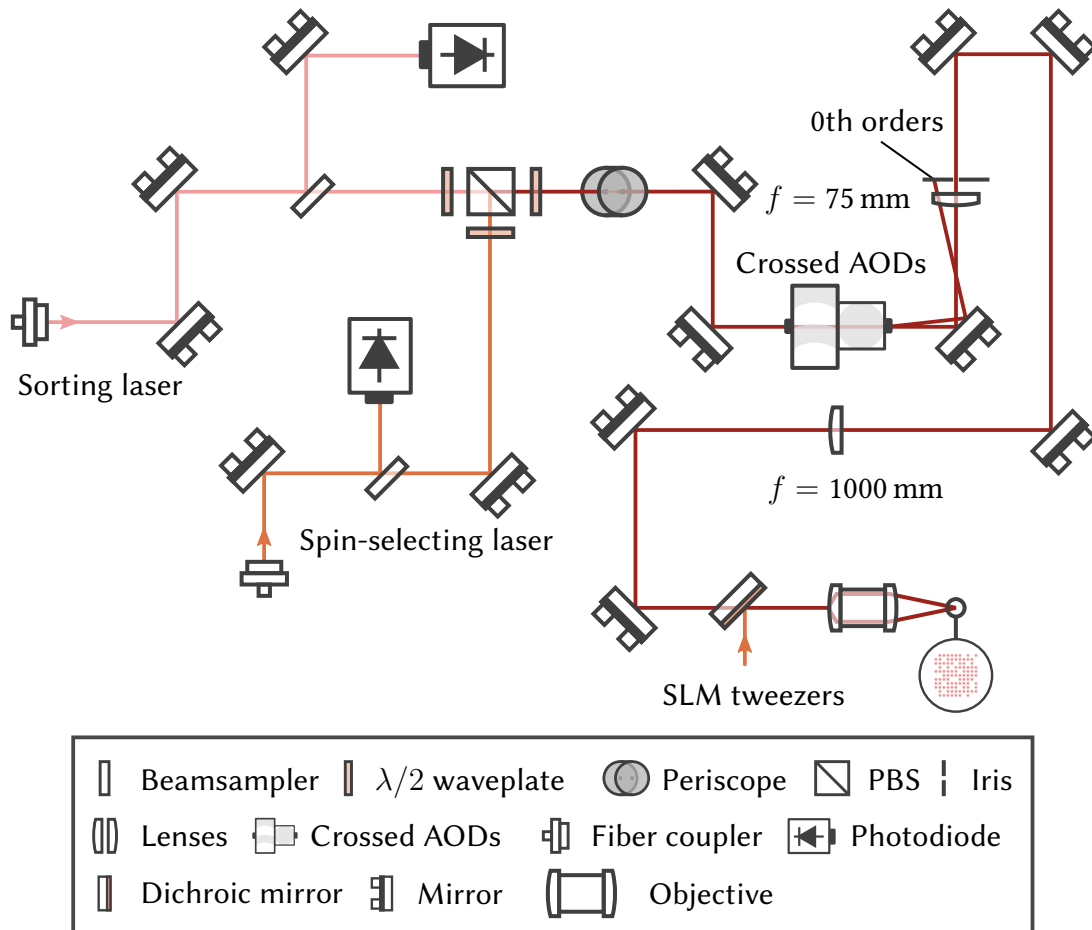


Figure 3.4.: Beam path to generate acousto-optically deflected tweezers. Two beams used for sorting and spin-resolved imaging are combined using a PBS. They pass the AOD after which the beam is shaped to match the objective into the experimental chamber.

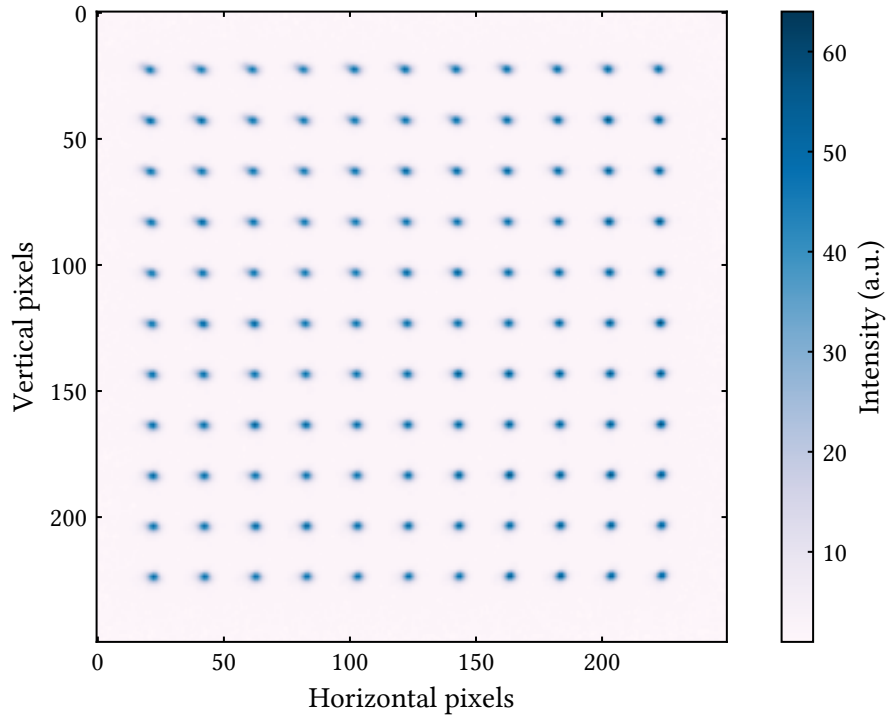


Figure 3.5.: An image of tweezers was acquired by activating a set of 11×11 frequency combinations on the crossed AODs. A slight field of view effect is visible in the top-left corner.

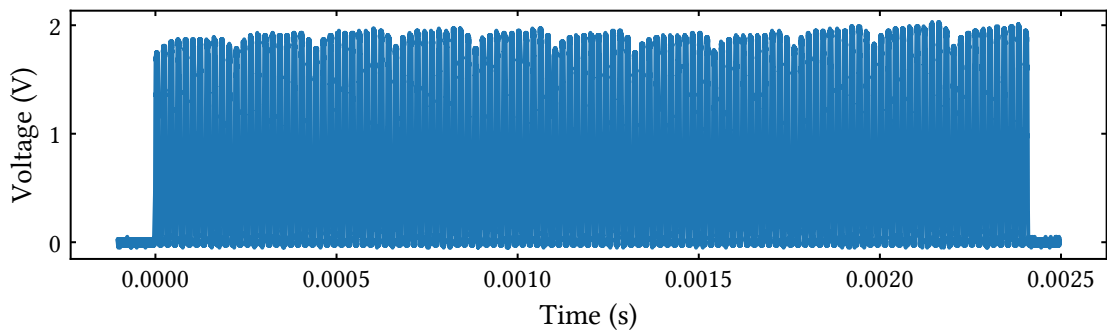


Figure 3.6.: The same tweezer picture as in Figure 3.5 was acquired using a photodiode. There is a trend of intensities growing towards the later tweezers. Between the last set of tweezers and the first, the difference is about 0.1 V or 5%.

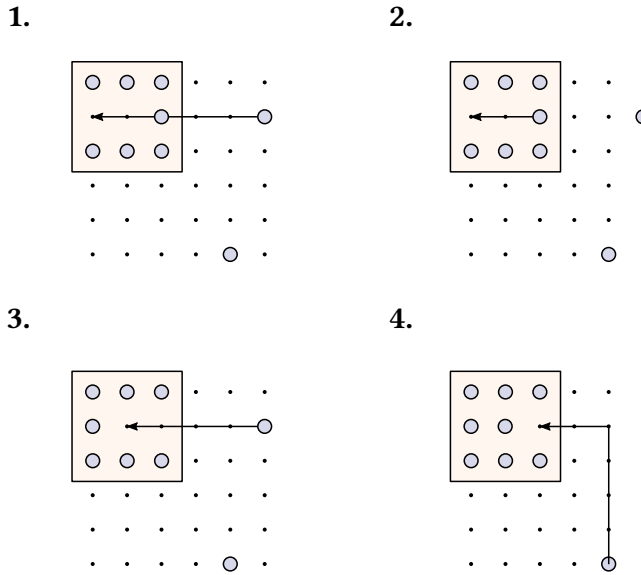


Figure 3.7.: Conceptual illustration of the pathfinding algorithm for resorting. The atom tries to move into a hole but has an obstacle (which is just another atom) in its way. The obstacle is first moved out of the way, after which the atom follows. The target area is then further filled with the remaining atom.

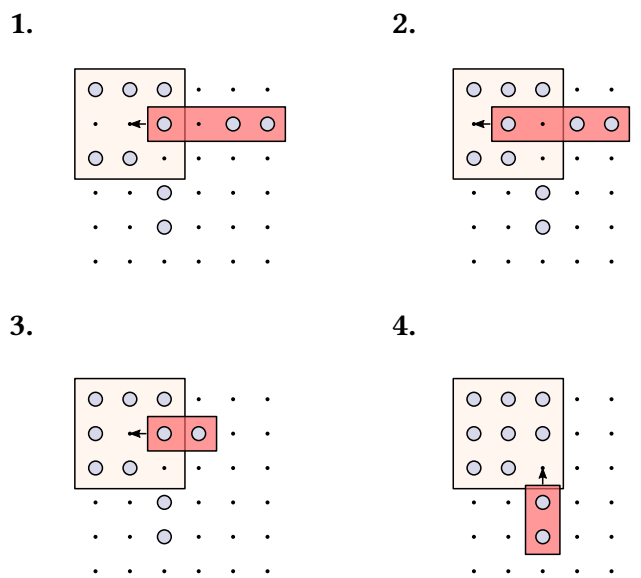


Figure 3.8.: Sorting atoms using the compression algorithm is done by selecting a full line of atoms. They are then moved towards the left edge. An atom that meets the edge is released before the others continue moving. When the steps for the rows have completed, the same process follows for the columns.

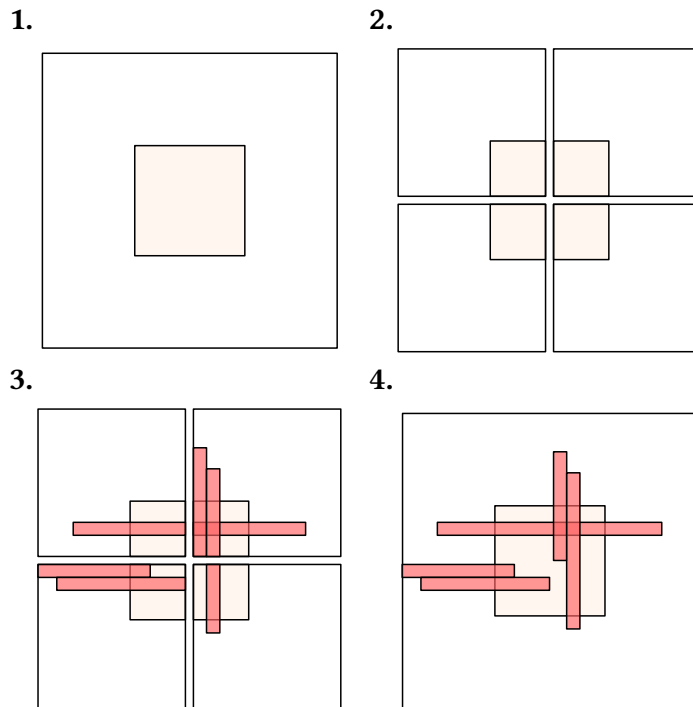


Figure 3.9.: Sequence of finding parallelized paths for the compression algorithm. Since atoms are always sorted into a corner, the compression algorithm can be split into four sections. The compression is run over each section, which finds the paths to move the atoms into a corner. In the last step, all paths that are in the same row or column, are combined and thus parallelized.

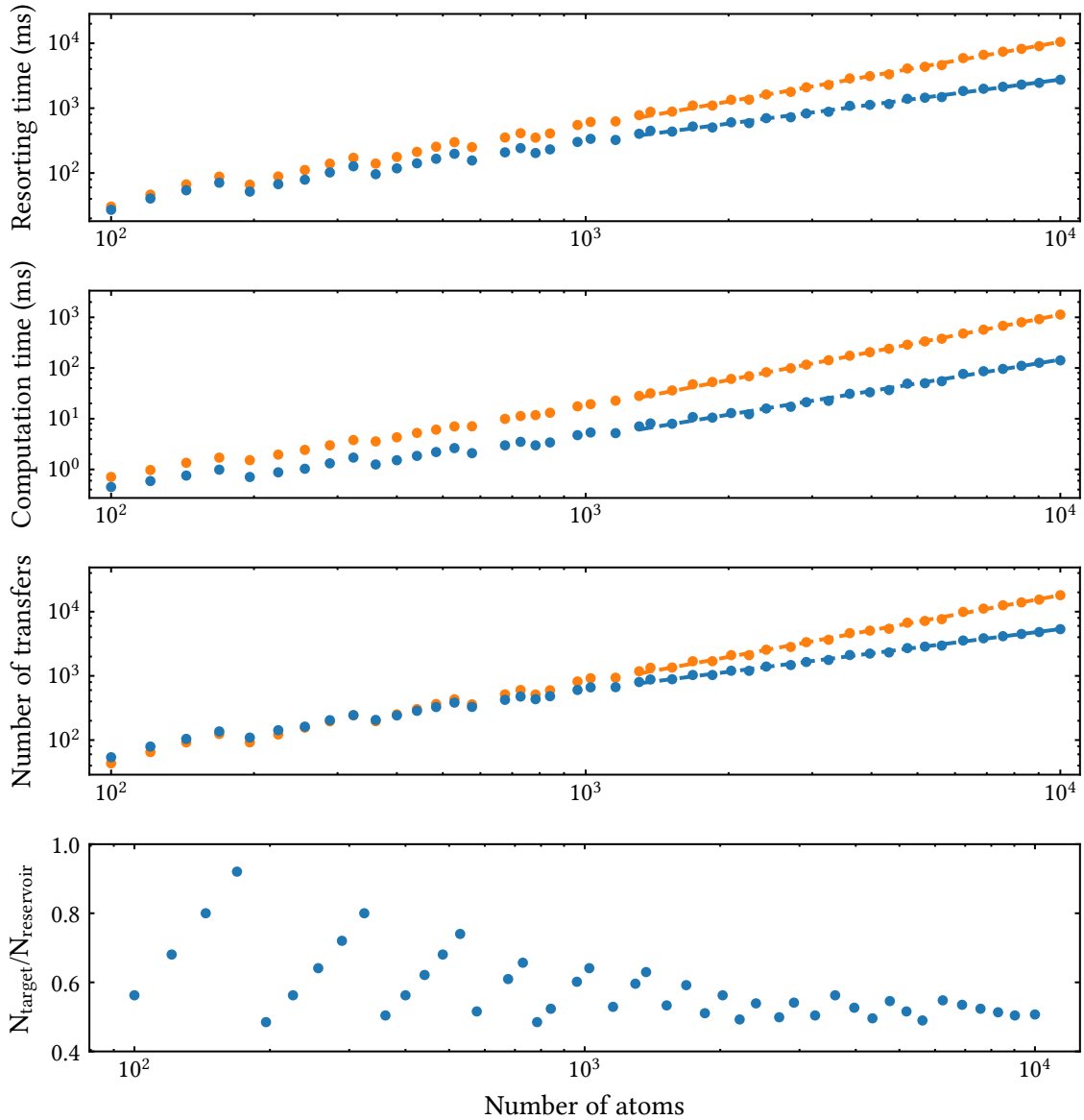


Figure 3.10.: Comparison of pathfinding algorithm (orange) and compression algorithm (blue) for sorting atoms into a target region. For each data point, 50 simulations were run and the mean of the result is shown. Standard deviation is on the size of the dots drawn and as such are not visible. The fraction of atoms in the target versus the reservoir area are shown in the last diagram. Since only integer values are allowed for the reservoir size, the fraction between the two sees a rounding effect. For this reason, the fit is only done for the upper half of the data points, where the effect is less pronounced. The values to the fit are given in Table 3.2.3.

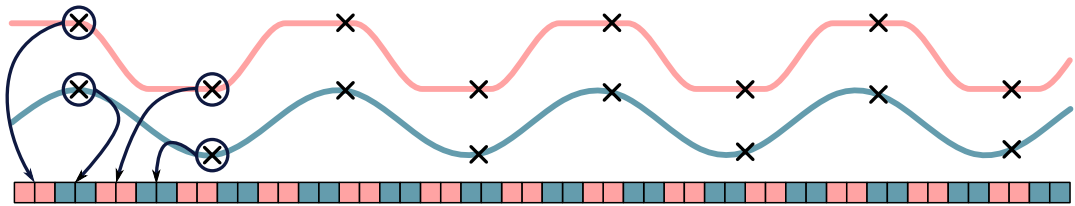


Figure 3.11.: Sampled data points are stored in a local buffer, which can then be transferred into the cards memory. The memory is effectively 1-dimensional, with two bytes for each sampled data point. Example signals are given for Channel 1 (red) and Channel 2 (blue). In the single replay mode, the data pointer will read from the first memory position until a given end point. In sequence replay mode, the data pointer will move forward, but can jump at any point based on user preference.

4. State selective light shifts for spin-sensitive imaging

Being able to measure the spin of ground state potassium atoms in many-body quantum experiments gives insight into the full quantum state and thus being able to pinpoint the ground state on the Bloch sphere. In Rydberg dressing experiments [23, 24], where the atom is in a ground state and fractionally in an excited Rydberg state, the spin can be used in a Ramsey sequence, in order to measure correlations [5, 25]. This is, since the ground state atoms in a superposition of two spins, couple to the Rydberg state. In order to measure effects, such as Rydberg blockade [11], and the resulting correlations, the superposition state acquires a phase on the Bloch sphere, which needs to be evaluated. This is currently achieved, by doing a projection measurement by removing one component out of the system.

With the new approach, it is possible to evaluate the spin species, by separating them in independent tweezers. A spin-sensitive tweezer array is then moved, and thus the atoms having this spin component follow this dipole potential. This creates a separation, and by evaluating the geometry from a fluorescence image, it is thus possible to find how the tweezer arrays were previously occupied. Measuring the spins this way, also means the atoms will not heat out during the process, and therefore the system can be reassembled and reused for further investigation.

if rydberg
dressing
wasn't dis-
cussed in
the Motiva-
tion, do it
here

The following chapter will discuss the setup in question in more detail, as well as the wavelength in use, in order to have tweezers sensitive to only one spin component. The new laser system is explained in detail, which includes a cavity for frequency stabilization, and therefore stability of the laser is discussed.

4.1. Approaches

Measuring the spin means in our experiment, to take a fluorescence image of the two ground states $F = 1$ and $F = 2$. However, during imaging, the spins are mixed, such that they can't be distinguished. As it was shown in Chapter 3, it is possible to move selected tweezers. Therefore two approaches are discussed in the following, both work by separating the two spins spatially. However, this requires finding ways of being sensitive to one specific ground-state spin. The first idea is using strong magnetic fields to increase the separation of the spin levels with the Zeeman effect. The second approach is using a state selective light shift, given by selecting a particular wavelength. This allows one spin component to be trapped, while the other will not see a trapping effect. In both applications, the idea is to trap one spin state in its own trap and physically move it away from the other. By taking an image, it is then possible to map positions to spins and therefore find out which tweezers contained which spin species. Moving the spin-sensitive tweezers back into its original position, the initial system is reassembled and new measurements can be taken with more information.

4.1.1. Zeemann induced potential separation

In the previous paragraphs, it was highlighted how the spin levels are too close in energy space, to address them with imaging lasers. However, having a position dependent potential, that is different for each spin state, is enough to spatially separate them. One way of achieving this, is by applying magnetic fields. In 1896, Pieter Zeeman wrote about how magnetic fields were affecting spectroscopy of atoms [26]. From this followed the Zeeman effect, which explains how spectral lines of atoms are split and shifted when applying magnetic fields. This can be calculated perturbatively [27], by modelling the atom as a magnetic dipole. In analaogue to the classic description of magnetic dipoles, this gives an energy V_M depending on the magnetic field \mathbf{B} :

$$V_M = -\mu \mathbf{B} \quad (4.1)$$

and is then the perturbation in the total Hamiltonian $H = H_0 + V_M$. The magnetic moment μ contains contributions from nuclear and electron spin, which then give direction and length of the magnetic dipole. The energy associated with the perturbation evaluates to

$$E_z = B_z \mu_B (g_l m_l + g_s m_s). \quad (4.2)$$

It has contributions from the nuclear spin ($g_l m_l$) and electron spin ($g_s m_s$) and depends on the Bohr magneton μ_B . The magnetic quantum numbers $m_i, i \in \{l, s\}$ depend on the value of the associated quantum numbers, which are the orbital angular momentum L and electron angular momentum S , such that $m_l \in \{-L, -L+1, \dots, L-1, L\}$ and $m_s \in \{-S, -S+1, \dots, S-1, S\}$. This means, not only is the hyperfine state shifted by the magnetic field, it is also split into more energy sublevels. However, a complete description of the energy shift, needs to integrate the shifts of the hyperfine levels, which has been done in the Breit-Rabi model [28].

Figure 4.1 gives an illustration of how the two spin components $F = 1$ and $F = 2$ in the potassium ground state are affected due to a magnetic field. Visible is a splitting of the spin-states into sublevels. In order to maximally separate the spin states, the $F = 1$ spin would be pumped into the $m_F = 1$ state, and consequently, $F = 2$ into the $m_F = 2$ state.

Using this, the idea is to create a position dependent trap for the two spin-states. To do this, we need to note, that from the figure, the $F = 1, m_F = 1$ state has a negative slope, while the $F = 2, m_F = 2$ state has a positive slope. This means, simply by generating a magnetic field ramp, the atoms in different spin states, will see a position dependent energy V_{mag} . Since the atoms are trapped inside optical tweezers, the potential given by the dipole force is [29]:

$$V_{dip}(r) = -\frac{\pi c^2 \Gamma}{2w_0^3 \Delta} I(r), \quad (4.3)$$

where Γ is the line width of the transition, in this case the D2 line, Δ the detuning, w_0 the resonance frequency and $I(r)$ the intensity of the laser beam. By applying the magnetic field gradient, the atoms see a total potential $V(r)$:

$$V(r) = V_{dip}(r) + V_{mag}(B(r)), \quad (4.4)$$

where the position dependence was explicitly noted. This way, the potential minimum, which was originally just given by the dipole trap, is now shifted in the direction of the

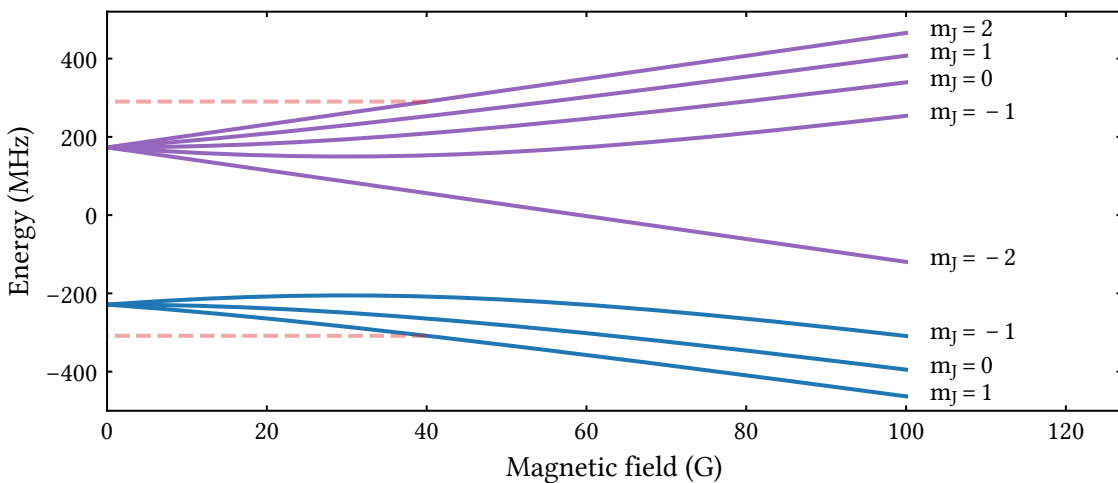


Figure 4.1.: The spectrum of ground state potassium is split into magnetic sublevels and shifted depending on a magnetic field applied to the atoms. Shown are two spin states $F = 1$ in blue and $F = 2$ in purple, relative to the ground state energy of $4\text{S}_{1/2}$.

potential induced by the Zeeman effect. Thus, the two spin states will see different potentials, which are shifted in position space with respect to each other. However, numerical calculations of the potential minimum show that the shift is too small in order to spatially separate the atoms. For this, it is assumed, the atom is trapped on the D2-line and the laser power is $1\text{ }\mu\text{W}$, where the spatial separation is favorable towards lower laser powers. Moreover, the magnetic field gradient is set to $B(r) = 40\text{ G cm}^{-1}$. This gives a separation of $\Delta x = 2.1\text{ nm}$, which is much less than typical beam waists of $w = 1\text{ }\mu\text{m}$. These results are further illustrated in Figure 4.2.

The parameters used in the calculations are already on the optimistic end, which leads to the conclusion that this approach only works when very high magnetic fields are applied. Simulations show, that applying a magnetic field slope of $B = 4000\text{ G cm}^{-1}$ results in a separation of $0.2\text{ }\mu\text{m}$. Luckily, there is another approach, which works by using only the light from frequency stable lasers, which is discussed in the following.

4.1.2. Utilization of state selective light shifts

The problem with the spin states being too close together still persists, however there is another effect that affects the energy of the spin states. Similar to the Zeeman effect, electrical

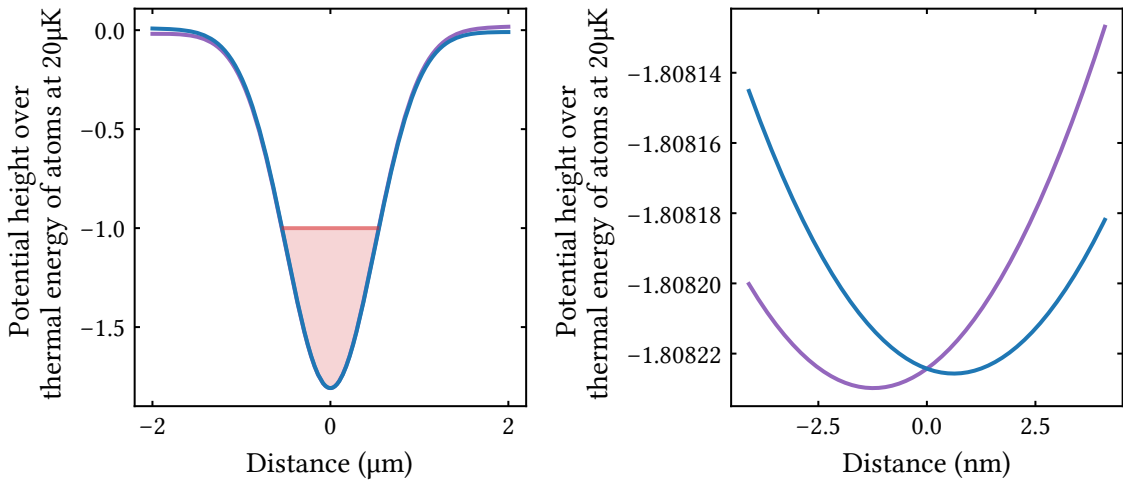


Figure 4.2.: Two spin species are subject to a dipole trap under the influence of a magnetic field gradient. The $F = 1, m_F = 1$ and $F = 2, m_F = 2$ states are colored in purple and blue respectively. The parameters for the trap are given in the text. Also shown is the energy of the atom as a red area. The zoomed in diagram on the right shows the separation of the two potentials, which is on the nanometer scale.

fields also shift and split energy levels [30, 31]. Under the influence of modulated electrical fields, such as coherent laser light, the effect is called AC Stark shift or simply light shift.

The shifts can be calculated by finding eigenenergies to the so-called Jaynes-Cummings Hamiltonian [32]. In it, the atom is described as a two-level system which has a resonance at w_a , as well as the being under the influence of a light field having a frequency w . Doing so, the Hamiltonian is written in three parts, containing the atomic resonance, light frequency and the interaction between both, resulting in:

$$H_{JC} = \hbar w_a \sigma^+ \sigma^- + \hbar w a^\dagger a + \hbar \frac{\Omega}{2} (a^\dagger \sigma^- + \sigma^+ a). \quad (4.5)$$

Here, the operators σ^+ , σ^- and a^\dagger, a refer to ladder operators of light and atomic levels respectively. The coupling strength is given by the vacuum Rabi frequency Ω , which depends on the electric field of the light and its polarization, as well as the dipole moment of the atom. By solving the Hamiltonian, the energy of the states is a shift to the vacuum energy shifts, depending on the principal quantum number n and is given as:

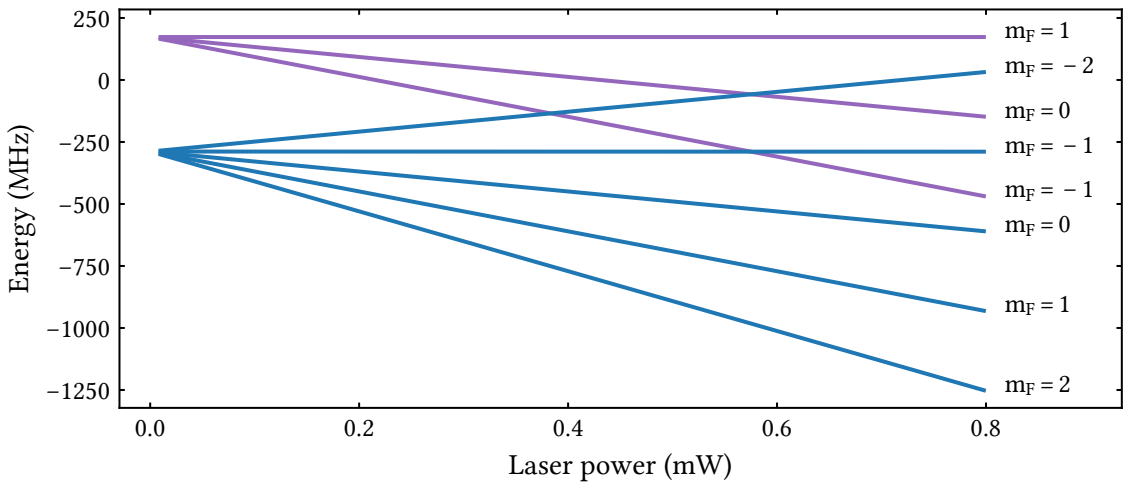


Figure 4.3.: The spin levels are split up due to the AC Stark shift from the laser illuminating the atoms. Shown are the ground states with $F = 1$ in purple and $F = 2$ in blue. The laser has a wavelength of 768.40 nm and positive circular polarization.

$$E_{JC} = \hbar \left(n + \frac{1}{2} \right) w \pm \frac{\hbar}{2} \sqrt{\Omega_n^2 + (w_a - w)^2}. \quad (4.6)$$

Here, the n-photon Rabi frequency is given as $\Omega_n = \Omega\sqrt{n+1}$. With these relations, it is instructive to see, that the electric field of laser light, and therefore simply the presence of a light field, induces light shifts on the atoms. Figure 4.3 shows the light shifts for the two spin states, $F = 1$ and $F = 2$ for the potassium atoms in the experiment.

Due to the light shifts, the atoms see an induced potential, given by the energy of the state. Therefore, the two spins can be spatially separated, when one component sees a potential, where the other one does not. This is easy to see in Figure 4.4, where the light shifts for the two spin states are given as a function of wavelength of the laser for circularly polarized light. We can see, that at 768.40 nm, the $F = 2$ state is trapped, while the $F = 1$ component does not see a light shift, which makes the atom with this spin transparent to the light.

In the experiment then, the light is produced as optical tweezers and mapped over the initial grid. To transfer the atoms into the spin-selective tweezer, the resulting trap has to be much deeper than the initial tweezers. These have a power of ≈ 15 mW, but are highly detuned to the excited state on the D2 line at a wavelength of 1064 nm. Moreover, due to laser light having a bandwidth, the transparent spin might actually see a trap, therefore it needs to be verified, whether this effect is non-negligible. Figure 4.5 shows the trap depth of

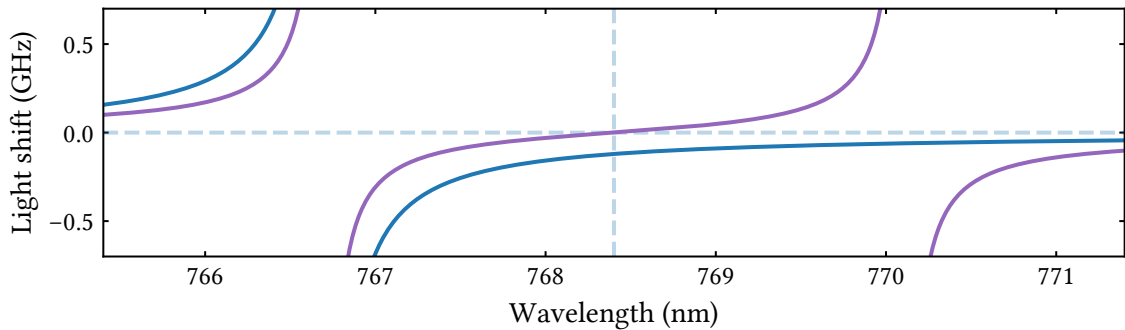


Figure 4.4.: The light shift of the $F = 1, m_F = 1$ (purple) and $F = 2, m_F = 2$ (blue) states against wavelength for a laser power of 0.1 mW and positive circular polarization. At 768.40 nm, the $F = 1$ component is transparent to the laser, therefore making it possible to trap only the $F = 2$ state.

the spin-sensitive tweezer over the trap depth of the initial tweezer, for both spin-species, when also accounting for a laser bandwidth of 100 GHz. It turns out, that the bandwidth does not majorly affect the efficiency of not trapping the transparent state. Consequently, using the AC-Stark shift to shift atom levels is a viable approach in order to trap a single spin-component, allowing to image specific spin states.

4.2. Setup

We have seen, how light shifts can be used to trap a single spin species. Doing so, it is possible to spatially separate and image them onto a camera. However, it is necessary to have a stable laser at 768.40 nm. The following section highlights the steps in order to build such a laser system, which includes setting up a cavity and a Pound Drever Hall (PDH) lock, in order to frequency stabilize the system. The laser is then coupled into the same setup as in 3, allowing to generate acousto-optically deflected, spin-sensitive tweezers, allowing to move the spin state in space.

4.2.1. Laser classification

The laser classified in the following is a homebuilt model, the design of which is given in Appendix ??_. It has room for a laser diode, whose light is collimated, filtered and reflected through a partially reflective mirror, which also serves as the output of the housing. The laser diode (Eagleyard EYP-RWE-0760-02010-1500-SOT12-0000) used, is tunable in the

ref

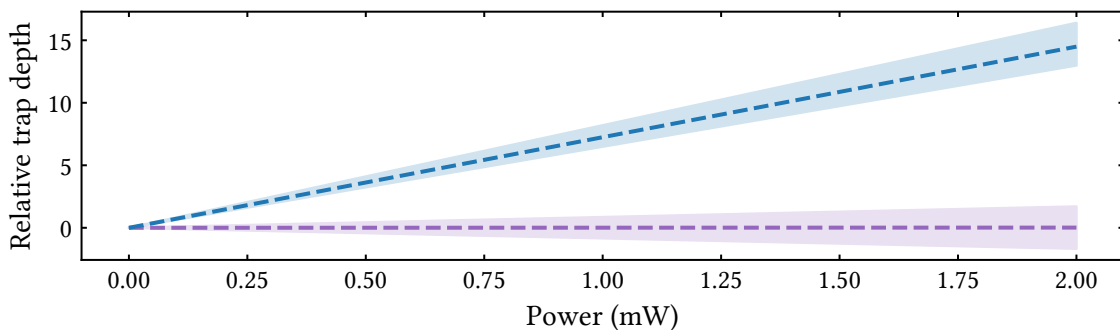


Figure 4.5.: Fraction of trap depths for the spin-tweezer and initial tweezers as a function of the spin-tweezer laser power. For the $F = 1, m_F = 1$ (purple) and $F = 2, m_F = 2$ (blue) state, only one state is trapped. Already at 2 mW power, the spin tweezer is more than 10 times deeper than the SLM tweezer. To argue that the bandwidth of the laser is not relevant for the efficiency of the spin-selective trapping, a bandwidth of 100 GHz was assumed and results in the shaded area surrounding the lines.

range from 752 nm to 772 nm with a maximum power of 80 mW. Since the diode is also used as the active medium, the cavity simplifies to being just a mirror, that reflects back into the diode and transmits part of the light out of the laser casing.

The laser power is classified as a function of current supplied to the laserdiode. After the laser threshold, the power is linear with current and the diagram for the model built here is given in Figure 4.6.

4.2.2. Beam setup of spin-selective laser

Now that there is a laser, the beam path in order to have a laser for spin-selective imaging can be set up. For this, two parts of the laser are split and coupled into fibers. One is used for monitoring of the wavelength, which will give an indication, if the frequency is currently locked or not. The second part will go to the cavity, allowing to actually perform the frequency stabilization. The full beam path is shown in Figure 4.7.

The main path is then coupled into a fibre, going towards the AOD discussed previously. However, the beam needs to be turned on and off at certain times during the experiment, for this, it first passes through an AOM and finally a shutter to block any leftover stray light. As shown previously, in 3.1.2, the light coming out of the fibre is then intensity stabilized and coupled into the AOD, which can be programmed to move the spin-sensitive tweezers.

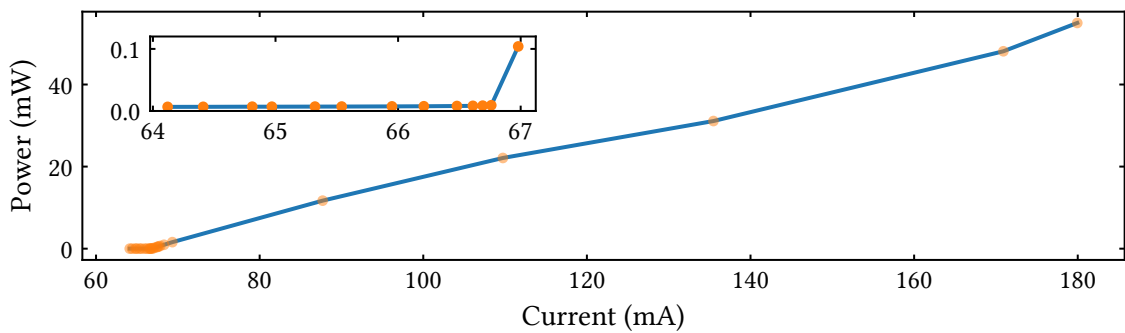


Figure 4.6.: Shown is the laser threshold for the home-built laser, driven with a Thorlabs LDC205C current controller. The power was measured using a Thorlabs PM100D power meter and the Thorlabs S121C sensor.

4.2.3. Cavity classification

The laser has been built and characterized and can be coupled into the AOD, in order to generate movable tweezer for spin-selective imaging. However, the process requires a stable frequency at 768.40 nm. As a matter of fact, not only are there resonances at 766.7 nm and 770.1 nm, this spin-selecting procedure works by requires that one spin state is completely transparent to the laser light, in terms of seeing a dipole potential. In order to have the laser emit a stable frequency, a piezo tunes the position of the mirror inside the laser cavity based on an input signal. This way, the length of the cavity, and therefore the standing wave, can be selected. However, pressure and temperature can both affect the mirror, and therefore there needs to be a system in place, to compensate for these factors.

Consequently, it is necessary to have a device, that measures the instability, and feeds back a signal to the piezo. In order to do so, a part of the laser is split off and sent into a stable cavity. The light that has passed the cavity is measured using a photodiode and it is then possible to measure resonances of this cavity. With the PDH method, an error signal is generated, that gives a feedback to the piezo. This generates a feedback loop, which is stable when the error signal is at a minimum. The process has been used and described in the experiment before [12]. The error signal recorded for this specific setup was recorded and is given in Chapter B.

The stable cavity in place for locking the laser frequency is made from a ultra-low expansion (ULE) glass, that has two mirrors attached to it. The material is not explicitly necessary, however the full extent of this specific ULE couldn't be used anymore, as only one side has the mirror contacted, while the other mirror is glued. Therefore, due to the glue, this cavity

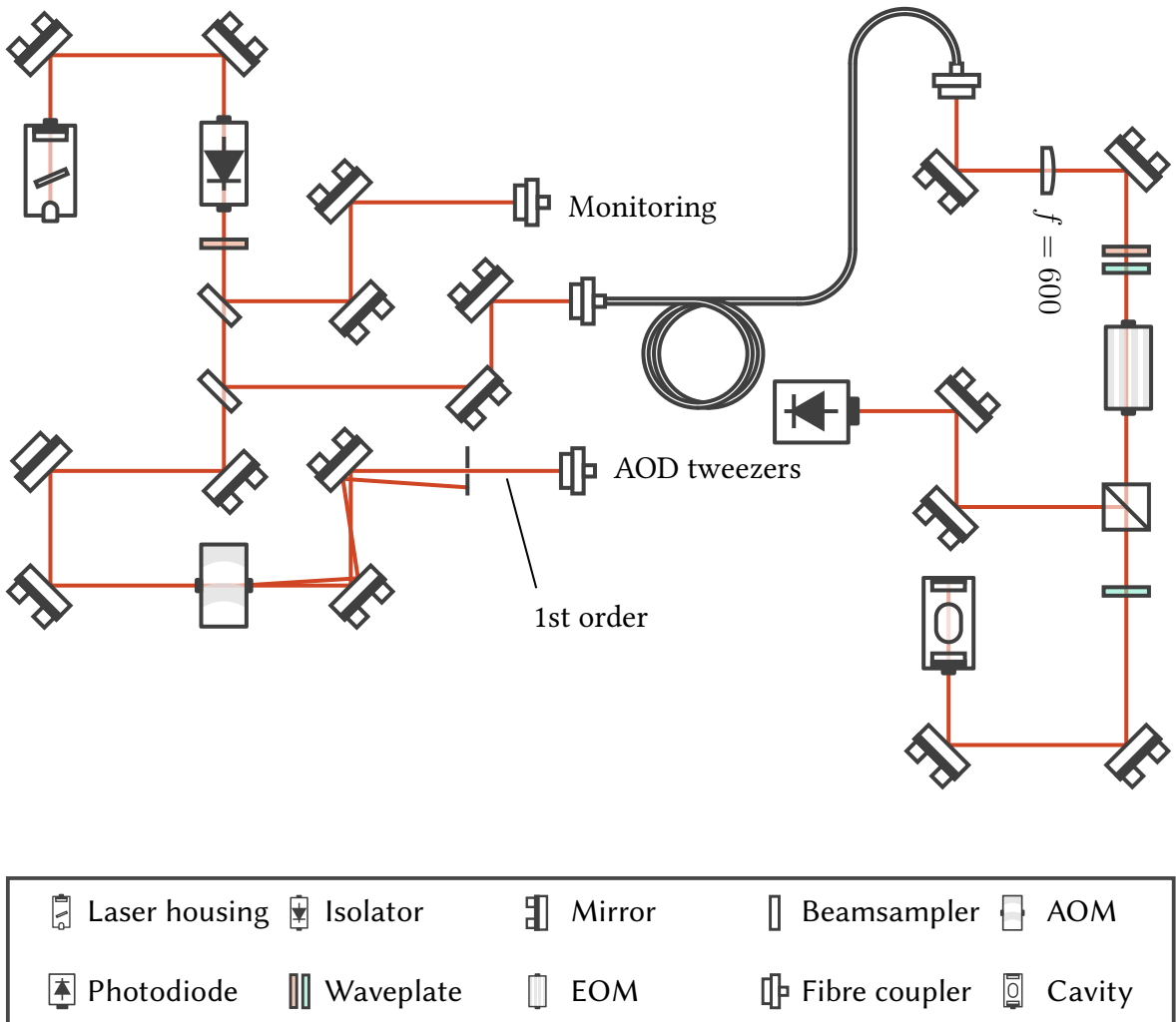


Figure 4.7.: Shown is the setup, in order to prepare the spin-sensitive tweezer for the experiment. The laser first passes an isolator, in order to protect the laser cavity from reflections. It is then split into two paths for monitoring and frequency stabilization. An AOD is used to switch the light on and off for the experiment.

is still prone to some wavelength drifts, induced by temperature expanding and compressing the material. This specific application can deal with these instabilities and therefore the glass was recycled for this setup. In order to stabilize the cavity against temperature fluctuations, it rests in a copper housing. This copper housing further rests in a stainless steel container. This container is then evacuated with a vacuum pump, which stabilizes the cavity against pressure fluctuations. A picture of the cavity is given in Appendix A.

In order to quantize the stability this cavity can provide, the frequency drift is measured. However, at 768.40 nm, the frequency is in the hundreds of terahertz, which is difficult to measure conventionally. However, by superimposing a reference laser onto the spin-laser, that has a very stable frequency, it is possible to measure the beat note. Mathematically,

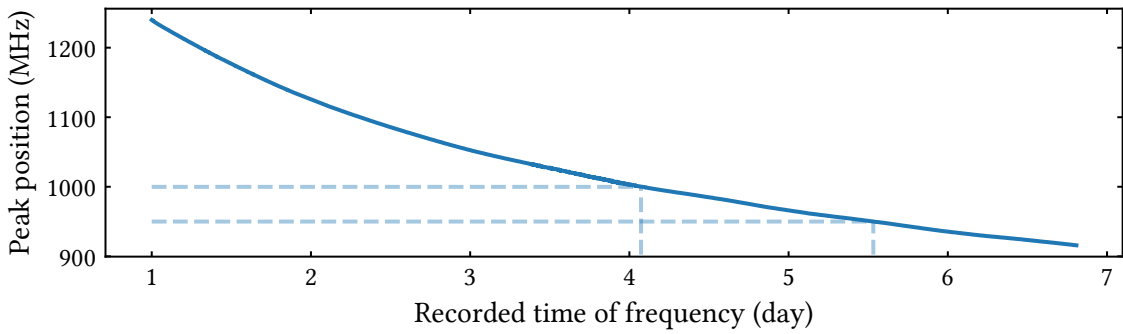


Figure 4.8.: The cavity drift was recorded over six days by doing a beat measurement with a reference laser. Horizontal lines show 50 MHz difference at the end of the measurement, where temperature and pressure has stabilized. From this it can be seen, that the drift is on the order of 33 MHz per day.

this means adding two sine-signals together:

$$\sin(2\pi f_1 t) + \sin(2\pi f_2 t) = 2 \sin\left(\frac{f_1 + f_2}{2}t\right) \cos\left(\frac{f_1 - f_2}{2}t\right), \quad (4.7)$$

where f_1 and f_2 are the frequencies of the reference and spin-laser respectively.

This relation turns two modulations, which have the frequencies added and subtracted. The first one still can't be resolved, however if the difference frequency is low enough, it is possible to see it on a spectrum analyzer. This means, the frequency of the "unstable" laser was first matched to the stable laser, such that the difference frequency was at least in the Megahertz regime. Then, it is possible to observe the drift of the cavity, which is the change in frequency with time. This usually happens due to temperature drifts affecting the cavity. The measurement was taken over several days and recorded as in Figure 4.8. Close to the end of the measurement, the drift was at a minimum of around 33 MHz per day, which is well within the limits, which can be verified with Figure 4.5.

With the cavity in place, all building blocks are there in order to separate spins of ground state potassium atoms. This means, the frequency stability given by the cavity locks the laser and makes it possible to position it close to the magic wavelength, where only one spin state sees a trap. By coupling the beam into the crossed AOD, each atom can be addressed and moved individually and an image of the spins can be acquired, while simultaneously keeping the atoms in the trap.

5. Conclusion and Outlook

This thesis discussed setups related to optical tweezer arrays in a Potassium-39 experiment. It was shown, how using a Pockels cell improves a current setup for loading atoms into SLM tweezers. With the new implementation, the duty cycle of the dipole traps during the chopping sequence can be increased, effectively improving the power available for every single tweezer. This also opens up the possibility of increasing the number of tweezer, as the trap depth available currently can then be distributed across a larger area. The discussion of sorting atoms followed, which solves the problem of only having 50% of sites occupied due to parametric heating. The solution requires moving atoms into unoccupied sites, which can be implemented using a pathfinding algorithm. As an alternative, a new algorithm was proposed, that uses parallelization and a digitizer card to move multiple atoms at the same time. The chapter was concluded by comparing the efficiency of the algorithms and by highlighting the requirements when using the digitizer card. The third setup then discussed an approach of doing spin-selective imaging, which will be useful in experiments involving Rydberg dressed states, as they are mostly ground states, but of unknown spin. For this, the spin states are spatially separated by using spin selective light shifts induced by a frequency stabilized laser. The laser system was built and characterized, and a stable cavity with a feedback loop to the laser for frequency stabilization was described. It is then coupled into the same crossed AODs used for the sorting, allowing to move atoms (and therefore the spin states) apart.

Shown were ways of improving the current state of the experimental setup. Moreover, there are applications beyond the scope of the current system in place. As was shown, the EOMs presented here also have faster repetition rates than the AOMs used currently. Apart from loading, it is then possible to drive faster pi-pulses in the experiment, or start doing Floquet engineering [33], which requires periodic driving of atoms. For sorting, being able to fill every site in an atomic array opens the door to manybody Rydberg effects. This allows for example to model antiferromagnets in an Ising-like system [34] and measure correlations without the need of heavy post-selection of data. It was motivated, how spin-selective imaging reduces cycle times, which ultimately leads to being able to take more statistics. This is a requirement to measuring entanglement entropies, for example Rényi

entropies [35] in a quantum information application of the experiment. Conclusively, the setups that were built over the course of this thesis offer a way to explore manybody Rydberg effects with high cycle times and high fidelity.

A. Cavity for frequency stability of spin-sensitive tweezer

A special cavity was built in order to stabilize the spin-sensitive tweezer against its frequency. The outer housing is made of stainless steel and can be evacuated using the flange in the back. The cavity is a ULE spacer, resting on a copper block, which should absorb most temperature instabilities. The spacer is surrounded by Viton rings, to prevent it from damage against direct contact with the copper block. Not visible are peek spacer between the copper block and steel casing, which isolate both parts from each other. A picture of the cavity is given below, in Figure A.1.

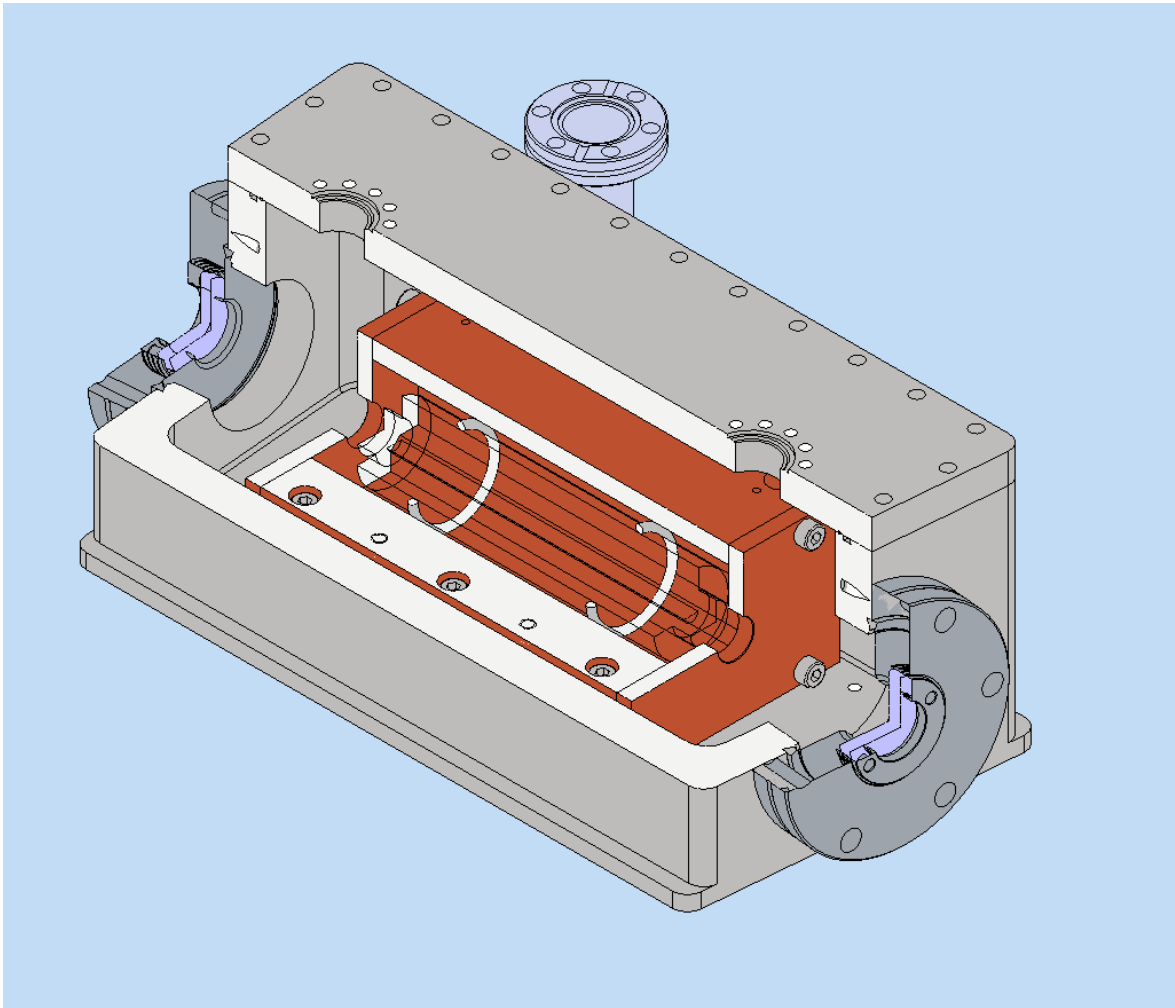


Figure A.1.: The cavity used for frequency locking the spins-sensitive tweezer.

B. PDH lock of cavity

Given below is the PDH locking signal retrieved, when scanning through the cavity.

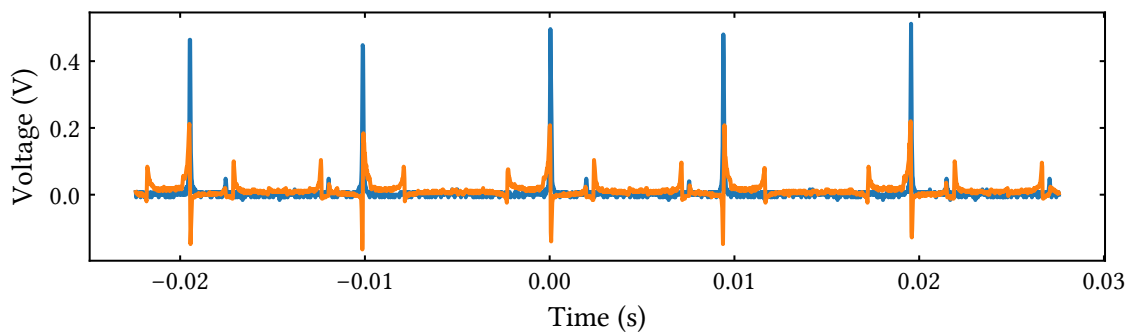


Figure B.1.: The PDH locking signal (orange) and the transmission signal of the cavity (blue).

Bibliography

1. Brewer, S. M. *et al.* Al+ 27 Quantum-Logic Clock with a Systematic Uncertainty below 10–18. *Physical Review Letters* **123**, 33201 (2019) (cit. on p. 1).
2. Anderson, M. H., Ensher, J. R., Matthews, M. R., Wieman, C. E. & Cornell, E. A. Observation of bose-einstein condensation in a dilute atomic vapor. *Collected Papers of Carl Wieman* **269**, 453–456 (1995) (cit. on p. 1).
3. Davis, K. B. *et al.* Bose-Einstein Condensation in a Gas of Sodium Atoms. *Phys. Rev. Lett.* **75**, 3969–3973 (1995) (cit. on p. 1).
4. Schauß, P. *et al.* Crystallization in Isingquantum magnets (2015) (cit. on p. 1).
5. Boll, M. *et al.* Spin- and density-resolved microscopy of antiferromagnetic correlations in Fermi-Hubbard chains. *Science* **353**, 1257–1260 (2016) (cit. on pp. 1, 43).
6. Bakr, W. S., Gillen, J. I., Peng, A., Fölling, S. & Greiner, M. A quantum gas microscope for detecting single atoms in a Hubbard-regime optical lattice. *Nature* **462**, 74–77. arXiv: 0908 . 0174 (2009) (cit. on p. 1).
7. Sherson, J. F. *et al.* Single-atom-resolved fluorescence imaging of an atomic Mott insulator. *Nature* **467**, 68–72 (2010) (cit. on p. 1).
8. Barredo, D., De Léséleuc, S., Lienhard, V., Lahaye, T. & Browaeys, A. An atom-by-atom assembler of defect-free arbitrary two-dimensional atomic arrays. *Science* **354**, 1021–1023 (Nov. 2016) (cit. on pp. 1, 17).
9. Endres, M. *et al.* Atom-by-atom assembly of defect-free one-dimensional cold atom arrays. *Science* **354**, 1024–1027 (Nov. 2016) (cit. on pp. 1, 17).
10. Norcia, M. A., Young, A. W. & Kaufman, A. M. Microscopic Control and Detection of Ultracold Strontium in Optical-Tweezer Arrays. *Physical Review X* **8**, 41054. arXiv: 1810 . 06626 (2018) (cit. on p. 1).
11. Urban, E. *et al.* Observation of Rydberg blockade between two atoms. *Nature Physics* **5**, 110–114. arXiv: 0805 . 0758 (2009) (cit. on pp. 1, 43).
12. Hirthe, S. *A Laser Setup for Two-Photon Rydberg Excitation of Potassium*, *Msc-thesis* tech. rep. (2018) (cit. on pp. 1, 51).

Bibliography

13. Osterholz, P. *Freely Configurable Holographic Trap Arrays for the Trapping of Single Atoms*, Msc-thesis tech. rep. (2020) (cit. on pp. 2, 3, 22) .
14. Salomon, G. *et al.* Gray-molasses cooling of 39K to a high phase-space density. *Epl* **104**. arXiv: 1310 . 4014 (2013) (cit. on p. 3) .
15. Hutzler, N. R., Liu, L. R., Yu, Y. & Ni, K. K. Eliminating light shifts for single atom trapping. *New Journal of Physics* **19** (2017) (cit. on p. 3) .
16. Saleh, B. E. A. & Teich, M. C. *Fundamentals of Photonics* (John Wiley & Sons, Inc., New York, USA, Aug. 1991) (cit. on pp. 6, 18) .
17. BME Bergmann. *Pockels Cell Driver Head* <https://web.archive.org/web/20200712183516/https://www.bme-bergmann.de/high-voltage-electronics/pockels-cell-driver-head/> (09/14/2020) (cit. on p. 12) .
18. Cooper, A. *et al.* Alkaline-Earth Atoms in Optical Tweezers. *Physical Review X* **8** (Dec. 2018) (cit. on p. 17) .
19. Barredo, D., Lienhard, V., de Léséleuc, S., Lahaye, T. & Browaeys, A. Synthetic three-dimensional atomic structures assembled atom by atom. *Nature* **561**, 79–82. arXiv: 1712 . 02727 (2018) (cit. on p. 17) .
20. Ohl de Mello, D., Birkl, G. & Walther, T. Rydberg interactions in a defect-free array of single-atom quantum systems (2020) (cit. on p. 25) .
21. Leseleuc, S. D. Quantum simulation of spin models with assembled arrays of Rydberg atoms (2018) (cit. on p. 30) .
22. NVIDIA. *Grafikkarten der GeForce 10-Serie* <https://www.nvidia.com/de-de/geforce/10-series/> (10/01/2020) (cit. on p. 33) .
23. Zeiher, J. *et al.* Many-body interferometry of a Rydberg-dressed spin lattice. *Nature Physics* **12**, 1095–1099. arXiv: 1602 . 06313 (2016) (cit. on p. 43) .
24. Borish, V., Marković, O., Hines, J. A., Rajagopal, S. V. & Schleier-Smith, M. Transverse-Field Ising Dynamics in a Rydberg-Dressed Atomic Gas. *Physical Review Letters* **124**, 1–6. arXiv: 1910 . 13687 (2020) (cit. on p. 43) .
25. Zeiher, J. *et al.* Coherent many-body spin dynamics in a long-range interacting Ising chain. *Physical Review X* **7**, 1–6. arXiv: 1705 . 08372 (2017) (cit. on p. 43) .
26. Zeeman, P. Ueber einen Einfluss der Magnetisirung auf die Natur des von einer Substanz emittirten Lichtes. *Verhandlungen der Physikalischen Gesellschaft zu Berlin* (1896) (cit. on p. 44) .

Bibliography

27. Griffiths, D. J. *Introduction to Quantum Mechanics (2nd Edition)* 2nd ed. (Pearson Prentice Hall, 2004) (cit. on p. 44) .
28. Breit, G. & Rabi, I. I. Measurement of nuclear spin [10]. *Physical Review* **38**, 2082–2083 (1931) (cit. on p. 45) .
29. Le Kien, F., Schneeweiss, P. & Rauschenbeutel, A. Dynamical polarizability of atoms in arbitrary light fields: General theory and application to cesium. *European Physical Journal D* **67**. arXiv: 1211.2673 (2013) (cit. on p. 45) .
30. Voigt, W. Ueber das Elektrische Analogon des Zeeman-effectes. *Annalen der Physik* **309** (1901) (cit. on p. 47) .
31. Courtney, M., Spellmeyer, N., Jiao, H. & Kleppner, D. Classical, semiclassical, and quantum dynamics in the lithium Stark system. *Physical Review A* **51**, 3604–3620 (1995) (cit. on p. 47) .
32. Fox, M. *Quantum optics: An Introduction* 1st ed. (2006) (cit. on p. 47) .
33. Oka, T. & Kitamura, S. Floquet engineering of quantum materials. *Annual Review of Condensed Matter Physics* **10**, 387–408. arXiv: 1804.03212 (2019) (cit. on p. 55) .
34. Lienhard, V. *et al.* Observing the Space- and Time-Dependent Growth of Correlations in Dynamically Tuned Synthetic Ising Models with Antiferromagnetic Interactions. *Physical Review X* **8**, 1–17 (2018) (cit. on p. 55) .
35. Wilde, M. M., Winter, A. & Yang, D. Strong Converse for the Classical Capacity of Entanglement-Breaking and Hadamard Channels via a Sandwiched Rényi Relative Entropy. *Communications in Mathematical Physics* **331**, 593–622. arXiv: 1306.1586 (2014) (cit. on p. 56) .

Statement of Authorship

I herewith declare that this thesis was solely composed by myself and that it constitutes my own work unless otherwise acknowledged in the text. I confirm that any quotes, arguments or concepts developed by another author and all sources of information are referenced throughout the thesis. This work has not been accepted in any previous application for a degree.

Munich, October 16, 2020

Signature